

EUMETSAT/ECMWF Fellowship Programme  
Research Report No. 47

# Assimilation of radiance observations from geostationary satellites: first year report

Chris Burrows

June 2018

Series: EUMETSAT/ECMWF Fellowship Programme Research Reports

A full list of ECMWF Publications can be found on our web site under:

<http://www.ecmwf.int/publications/>

Contact: [library@ecmwf.int](mailto:library@ecmwf.int)

©Copyright 2018

European Centre for Medium Range Weather Forecasts  
Shinfield Park, Reading, RG2 9AX, England

Literary and scientific copyrights belong to ECMWF and are reserved in all countries. This publication is not to be reprinted or translated in whole or in part without the written permission of the Director-General. Appropriate non-commercial use will normally be granted under the condition that reference is made to ECMWF.

The information within this publication is given in good faith and considered to be true, but ECMWF accepts no liability for error, omission and for loss or damage arising from its use.

## Executive summary

This report summarises the work carried out during the first year of this EUMETSAT Fellowship. The contents of the three sections that comprise this report are described briefly here.

### *Changes to the geostationary network*

In 2017/18 there have been a number of important changes to the set of geostationary satellites that provides clear-sky radiance (CSR) or all-sky radiance (ASR) products, which are assimilated at ECMWF.

In January 2018, GOES-13 was retired from the operational GOES-EAST service and its successor, GOES-16 (launched in November 2016) is the first to carry the Advanced Baseline Imager (ABI) with significantly improved spatial, spectral and temporal sampling. We have worked closely with NOAA NESDIS to accelerate their provision of CSR/ASR products from the new satellite in order to minimise the period with no operationally-assimilated GOES-EAST radiances ahead of the onset of the 2018 Atlantic Hurricane season. Real time GOES-16 radiances were ingested passively into the ECMWF system in May 2018 and early evaluations suggest the quality of the radiance observations is very good.

In February 2018, Meteosat-11 replaced Meteosat-10 as the EUMETSAT “0 degree service”. The absence of an exact overlap-period where both satellites were stationary meant that a short gap in the assimilation of data was unavoidable, but delays were successfully minimised and radiances from Meteosat-11 were assimilated operationally at ECMWF by 20 February 2018.

The Japanese satellite Himawari-9, the replacement for Himawari-8, was launched in November 2016, and will remain in on-orbit storage until Himawari-8 reaches its end of life (2029) or encounters problems in the meantime. A sample of radiance data from Himawari-9 has been made available to users and generally compares well with similar data from Himawari-8.

### *Research to maximise the impact of geostationary radiance data*

During the period when Meteosat-10 and Meteosat-11 were manoeuvring to adopt their new positions, small systematic residual bias patterns were observed in the radiance data in the east-west direction. Similar biases (though in the north-south direction) were observed for the high-inclination Meteosat-8. This may be an artefact of the image rectification, and to assimilate these data optimally, the biases should be accounted for.

Research experiments have shown that much more geostationary data near the edge of the discs can be successfully assimilated, aided by slant-path radiative transfer. By extending the zenith angle limit from 60° to 74°, and applying slant path radiative transfer, the additional observations have been shown to improve NWP analyses and forecasts.

Improvements in analyses and forecasts have also been obtained by assimilating geostationary radiances with a more sophisticated description of observation error. Applying the technique proposed by Desroziers [Desroziers et al. \[2005\]](#), observation errors for all water vapour channels have been refined and full inter-channel correlations diagnosed.

*Future work*

The most immediate task is to finalise assimilation testing and implement radiance products from GOES-16 in operations. Preparations will also be made for the ingest and assessment of data from GOES-17 (intended to replace GOES-15 as GOES-WEST).

GOES-16 provides radiance data from the full disc every 15 minutes and observational data with this degree of spatial coverage and temporal resolution offers promising opportunities for greatly enhanced 4D-Var wind tracing. This will be investigated as a priority given the similarly frequent coverage anticipated from MTG-IRS.

A related avenue of research will test assigning different observation errors to data depending on their time position in the 4D assimilation window. The rationale will be to account for integration of the forecast model (as part of the observation operator) being a potentially dominant component to the total assigned uncertainty.

Finally, obtaining and analysing observations from the hyper-spectral GIIRS instrument on the Chinese satellite FY-4A remains a high priority in order to prepare for hyper-spectral data from MTG-IRS.

# 1 Changes to the geostationary network

## 1.1 Retirement of GOES-13

### 1.1.1 Introduction

GOES-13 was launched in 2006 and became the operational GOES-EAST satellite on April 14, 2010; its orbit was at around  $75^\circ$  West and it provided data from the Americas, the eastern Pacific and western Atlantic. At ECMWF, assimilation of clear sky radiance (CSR) data from the  $6.55\mu\text{m}$  water vapour (WV) channel of the IMAGER instrument on GOES-13 began 14 days after it was declared operational. Since then, brightness temperatures from this instrument have been assimilated with only minor interruptions. The next generation satellite GOES-R (GOES-16) became the operational GOES-EAST service on December 17, 2017 and GOES-13 was retired three weeks later, on January 8, 2018.

The method for assimilating CSR data at ECMWF has been documented in earlier EUMETSAT Fellowship reports and articles (Köpken et al. [2003], Munro et al. [2004], Letertre-Danczak [2016a]), but a brief summary is provided here for context:

CSR brightness temperatures are thinned to around 100km, depending on latitude. The CSR data themselves are averages of the clear pixels that comprise each “super-ob” which is typically produced from boxes of 16x16 pixels. The percentage of clear pixels that contribute to each CSR value is also provided. Over land, observations are rejected if this value is less than 70% in order to reduce the effect of any residual cloud contamination which can affect the products. Over sea, instead, the magnitude of the first guess departure (observation minus background) of a window channel is used to check for undetected cloud; if the magnitude of this value is greater than 3K it is indicative of the presence in cloud in either the background field or the observations, so these observations are rejected. The WV channel observations are assimilated with 2K observation errors. Figure 1 shows the Jacobians of the GOES IMAGER instrument.

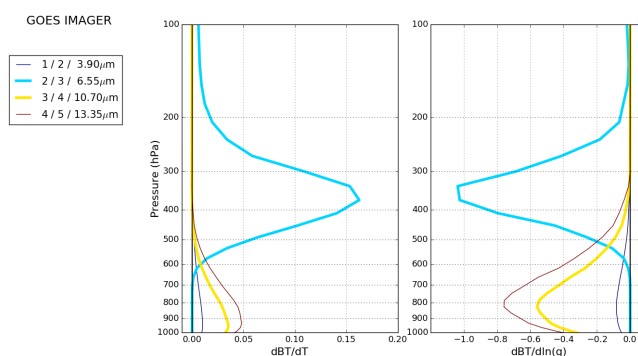


Figure 1: Temperature and water vapour Jacobians for the thermal IR channels of the GOES IMAGER.

In preparation for the retirement of GOES-13, a blacklist change was made to reject all CSR data from this satellite from December 14 2017 onwards. Originally, this was the day on which the data service from GOES-13 would terminate, but this was extended. The rejection still occurred on December 14. At the time of writing, real-time, official GOES-16 CSR data has still not be delivered and this will be discussed in more detail in section 1.4. Although the coverage of the geostationary satellites has a degree

of overlap, there is still a gap present (see Figure 2).

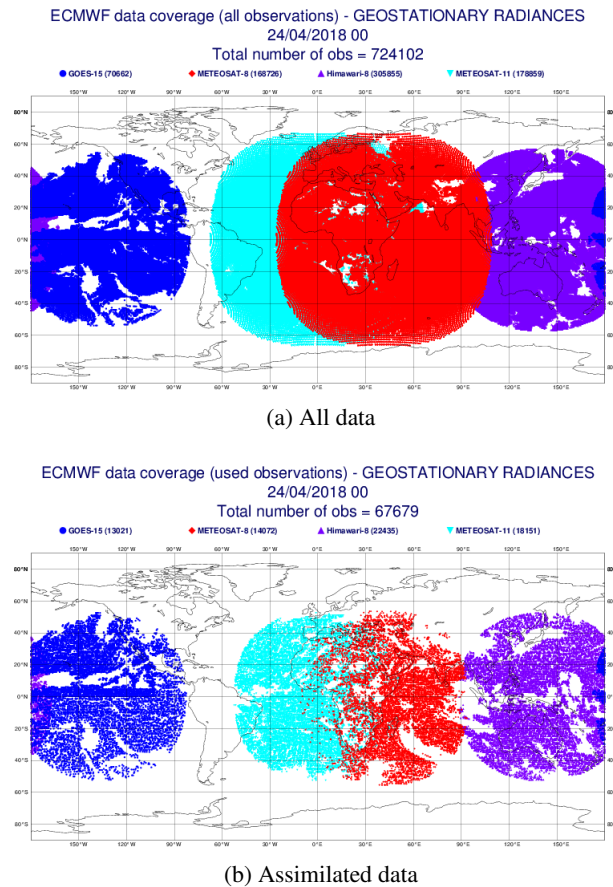


Figure 2: Coverage of (a) all available geostationary CSR/ASR data and (b) all assimilated data from a six hour window centred at 00Z on April 24 2018. This demonstrates the effect of thinning, cloud-clearing and the restriction imposed on the zenith angles of the observations.

### 1.1.2 Impact of GOES-13

An experiment has been run to assess the impact of losing data from GOES-13. The experiment was performed for the period 1/4/17 to 29/5/17, and *all* data was removed from the system in the experiment, i.e. both radiances and atmospheric motion vectors (AMVs). The effect on the forecast RMS errors at medium range is quite neutral, though there is a statistically significant impact in the first guess fits to other observation types. See Figure 3 for examples of the change to the first-guess departures of independent observations which show a statistically significant effect.

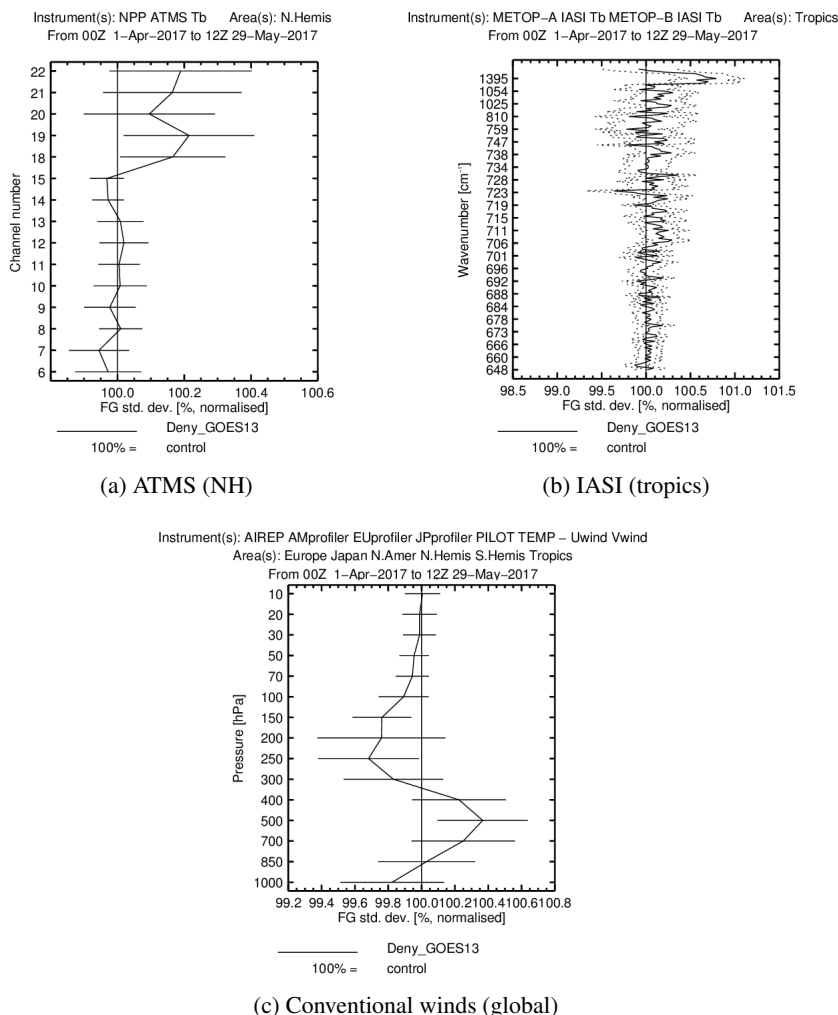


Figure 3: First guess departure statistics showing the effect of removing GOES-13 data (both CSRs and AMVs) from the ECMWF NWP system. The first guess fit to the ATMS WV channels is degraded in the northern hemisphere (a) which is consistent with the removal of the WV-sensitive CSRs. Similarly, the first guess fit to the IASI WV channels is degraded in the tropics (b). The fit to conventional wind observations (c) is also modified, presumably as a response to the rejection of the AMVs, plus the wind-tracing effect of the CSRs.

The degradation in the fit to the ATMS and IASI WV channels is significant, and is consistent with other denial experiments of geostationary CSR/ASR data (not shown), and indicates that at the short-range, the absence of CSR data from GOES-13 is detrimental to the forecast of tropospheric water vapour. The impact on the conventional wind observation is more mixed, showing a degradation around 500hPa and an improvement at around 250hPa. Without running separate experiments rejecting CSRs and AMVs separately, it is difficult to attribute the 250hPa degradation to one of the observation types, but both radiances and AMVs from the WV channel on the GOES images are assimilated, so it is possible that some information is being assimilated twice, in separate forms, without accounting for correlations between their errors. For example, it is known that the 4D-Var is able to provide wind increments indirectly from the assimilation of the radiances, as well as directly from the AMVs (Peubey and McNally [2009]).

## 1.2 Transition from Meteosat-10 to Meteosat-11

### 1.2.1 Plans

Meteosat-10 was the prime full Earth scan (FES) service over  $0^\circ$  longitude, and was first assimilated at ECMWF in January 2013. This was the first instrument from which all sky radiance (ASR) data were used, whereby, in addition to assimilating clear sky radiances, observations from fully overcast scenes were also assimilated with an extended 4D-Var control vector to retrieve cloud information (Lupu and McNally [2012]). Note that this is not a true all-sky approach as the retrieved cloud parameters are independent of cloud information within the model, and so the model cloud parameters are not incremented via the adjoint of the observation operator. Meteosat-11 is the successor to Meteosat-10 and is the final Meteosat Second Generation (MSG) satellite. Like its predecessor, Meteosat-11 carries a SEVIRI instrument. The transition to Meteosat-11 occurred early in 2018.

The key events were that; on 30/1/18, Meteosat-11 ASR data became available to NWP centres, and on 6/3/18, Meteosat-10 ceased producing full disc scans. Unfortunately, there was no period of exact overlap between the two satellites; initially, Meteosat-11 was at  $3.5^\circ\text{W}$  and its drift to  $0^\circ$  occurred from 5/2/18 to 13/2/18. Similarly, Meteosat-10 drifted from  $1^\circ\text{E}$  to  $9.5^\circ\text{E}$  from 8/2/18 to 25/2/18 (the sub-satellite longitudes are plotted for the two satellites in Figure 4). Were it not for the drifts, this would still have been a demanding transition for NWP users, where longer periods of overlap are desirable in order to perform direct comparisons between the outgoing and incoming satellites. The time frames are summarised in Figure 5. Before the transition took place, a plan was prepared for how to handle the data during the transition. In particular, there was concern about using the data while the satellites were drifting. The plan was as follows, and the same plan was applied for both ASRs and AMVs:

- Begin assessing data from Meteosat-11 as soon as it became available (30/1/18).
- Reject Meteosat-10 from operations before it begins to drift to its new position (7/2/18).
- Begin passive monitoring of Meteosat-11 (to spin up VarBC predictor coefficients) at the end of the drift (13/2/18).
- Begin active assimilation of Meteosat-11 after a week of spin-up (20/2/18).

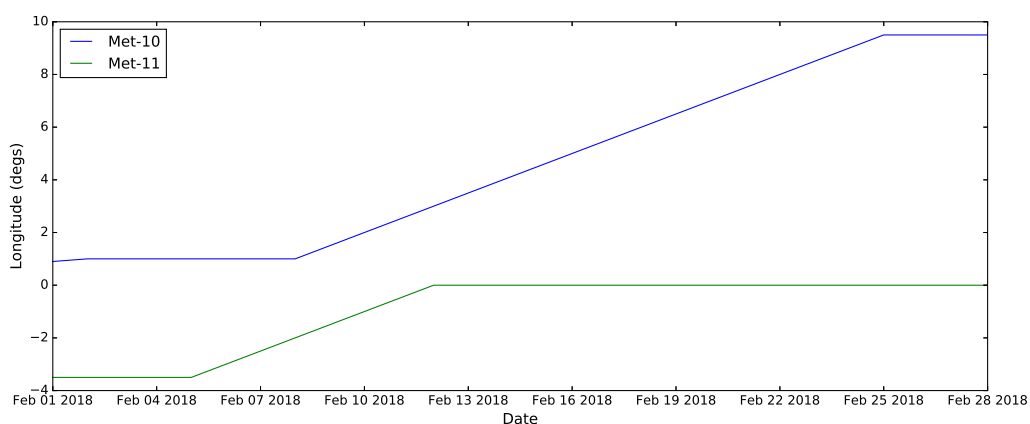


Figure 4: Sub-satellite longitudes of Meteosat-10 and Meteosat-11 during the February 2018 drifts.

This plan did include a period where neither satellite was being assimilated, but this was deemed a reasonable forfeit given that both satellites would be drifting during this period, despite the fact that data from GOES-EAST were not available for assimilation, so no geostationary data from the north Atlantic region were being assimilated during this 12 day period.

Previously, a preliminary assessment of Meteosat-11 was performed on test data supplied by EUMETSAT (Letertre-Danczak [2016b]), demonstrating that the ASR data had similar quality to Meteosat-10, so this gave the confidence to anticipate that the VarBC spin-up would proceed satisfactorily.

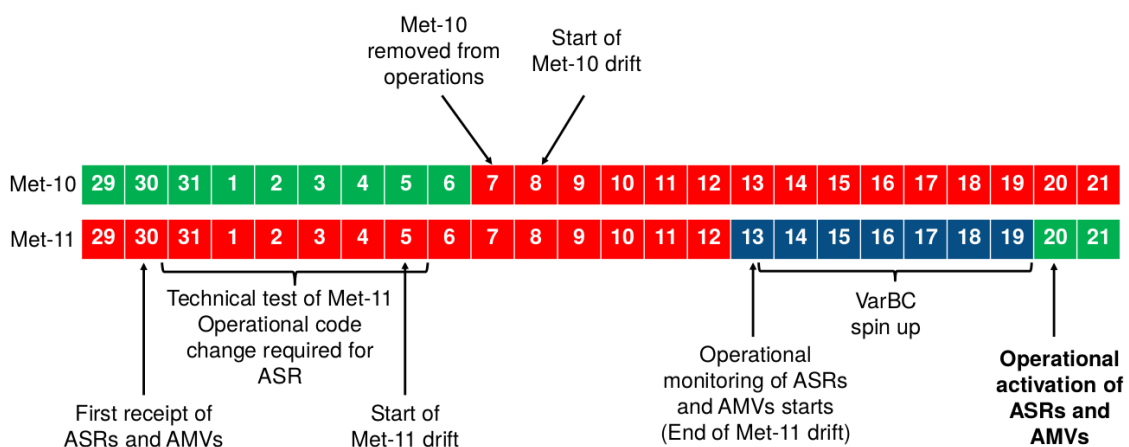


Figure 5: Timetable for January to February 2018 illustrating the data usage during the transition from Meteosat-10 to Meteosat-11. Green indicates when observations were actively assimilated, red indicates that they were rejected, and blue indicates that they were being “passively monitored”, i.e. VarBC coefficients were being computed in operations, but the observations themselves were not actually being assimilated.

### 1.2.2 Rejecting Meteosat-10

A time series of first guess departures of Meteosat-10 from February 2018 shows some interesting features (Figure 6).

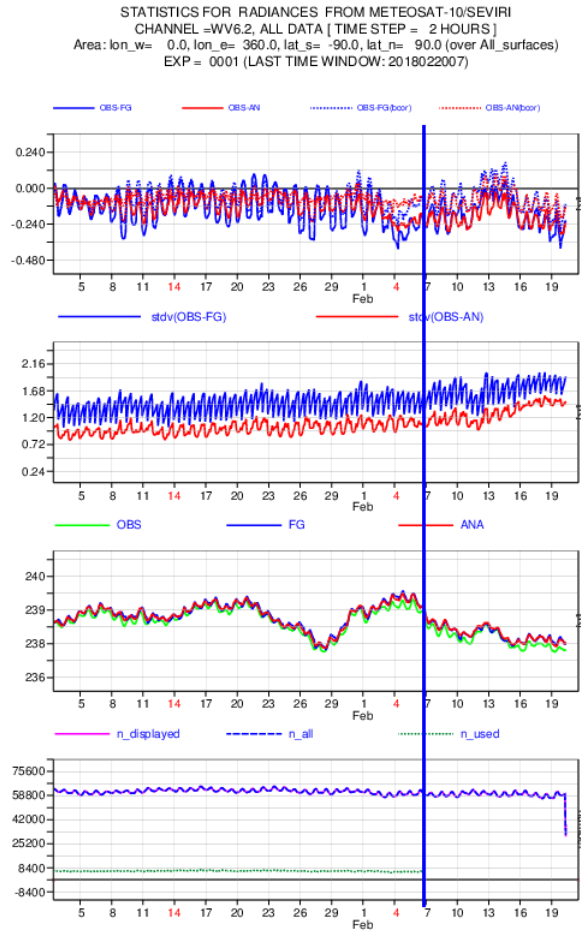


Figure 6: Time series of first guess and analysis departures for Meteosat-10 ASR observations from the  $6.2\mu m$  WV channel. These data were assimilated up to 7/2/18 (marked by the vertical blue line), after which date the satellite began to drift and was rejected from operational assimilation.

When the Meteosat-10 radiances were rejected from the assimilation, the standard deviation of the first guess departures began to increase. This is likely due to a combination of two effects. Firstly, the analysis fields will have been degraded due to the lack of Meteosat-10 data being assimilated (both ASRs and AMVs), and so the increased errors in the analyses will propagate through to the backgrounds. Secondly, the satellite was drifting during this period, so this may contribute to the gradual increase in standard deviations as the longitude of the sub-satellite point drifted further from  $0^\circ$  (see Section 2.1 for more discussion about this potential source of error). A Hovmöller plot of the standard deviations of Meteosat-10 first guess departures clearly shows that as soon as Meteosat-10 is rejected from the assimilation, there is an increase in the tropics, and as the drift proceeds, these values increase, as do those at higher latitudes (see Figure 7).

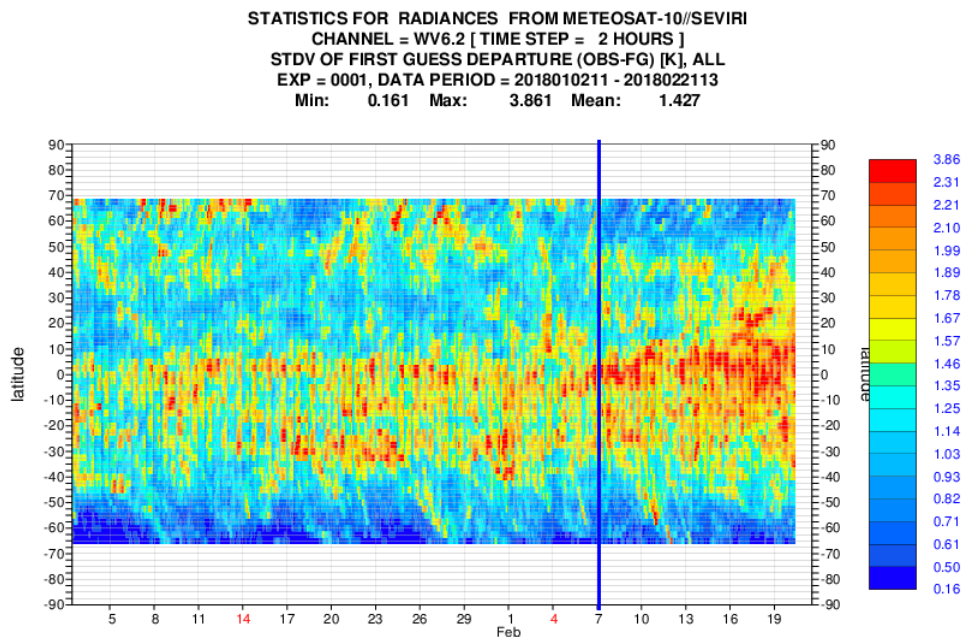


Figure 7: Hovmöller plot of the standard deviations of first guess departures for Meteosat-10 ASR observations from the  $6.2\mu\text{m}$  WV channel. These data were assimilated up to 7/2/18 (marked by the vertical blue line), after which date the satellite began to drift and both ASRs and AMVs were rejected from operational assimilation.

It is worth remembering that both ASRs and AMVs were rejected at the same time, so the initial degradation in first guess fields is likely to be due to the absence of both observation types. The gradual increase from that date onwards is likely to a combination of the satellite's drift and the diminishing effect of any residual impact from assimilating the observations.

The first guess departure statistics for Meteosat-8 provide a somewhat contrasting picture — this satellite has a large degree of overlap with Meteosat-10 (see Figure 2), and the instrument is nominally identical. Therefore, it can act as a fairly independent measure of the effect that the lack of Meteosat-10 has on the first guesses. Before assessing the statistics, it should be noted that the SEVIRI ASR observations are thinned together, so when Meteosat-10 is rejected, the number of Meteosat-8 observations assimilated on the western edge of the disc increases. Looking at Figure 8 (whose statistics include non-assimilated data) it can be seen that the standard deviation of Meteosat-8 first guess departures increases at low- and mid-latitudes when Meteosat-10 is rejected. Interestingly, there appears to be a significantly improved first guess fit to the observations above about  $45^\circ$  North, and this is also present to a lesser extent in Figure 7. ASR data are only assimilated up to zenith angles of  $60^\circ$  which, for a satellite above the equator corresponds to a maximum north-south limit of  $\pm 52^\circ$  latitude (see Section 2.2 for more details regarding this limit). However, the AMVs are assimilated up to zenith angles of  $65^\circ$  which corresponds to a maximum north-south limit of  $\pm 57^\circ$  latitude, so it is possible that the apparent degradation in the passive ASR monitoring at high latitudes is related to the AMVs or the way in which the wind observations may be interacting with the ASRs in the 4D-Var.

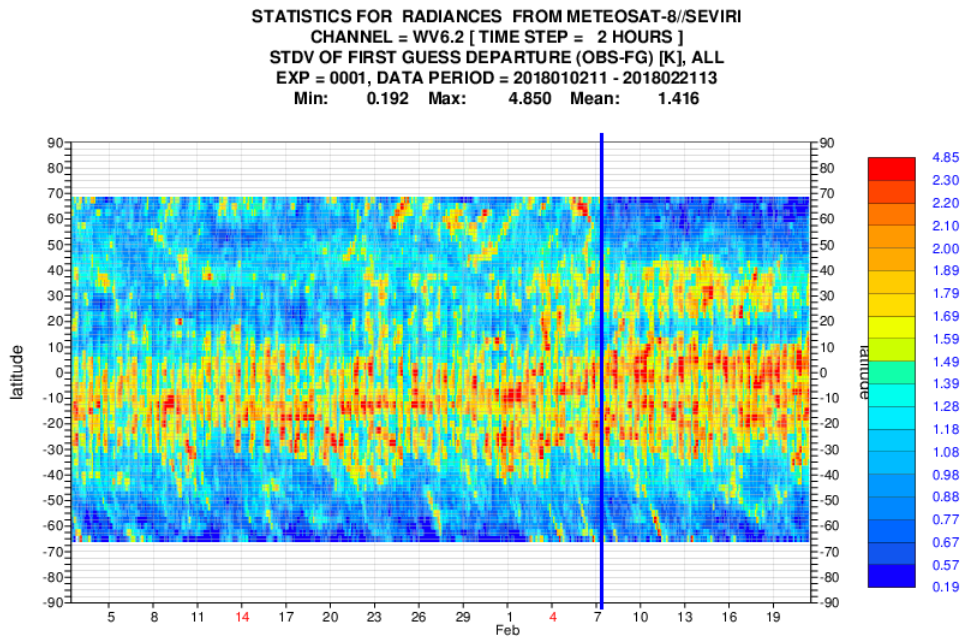
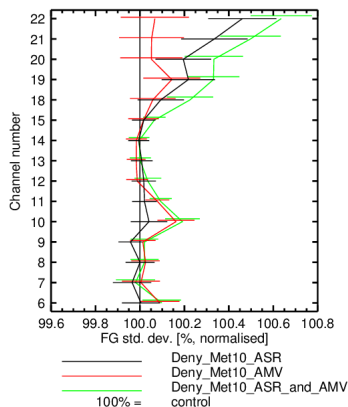


Figure 8: Hovmöller plot of the standard deviations of first guess departures for Meteosat-8 ASR observations from the  $6.2\mu\text{m}$  WV channel. Meteosat-10 data were assimilated up to 7/2/18 (marked by the vertical blue line), after which date the satellite was rejected from operational assimilation.

### 1.2.3 Impact of Meteosat-10

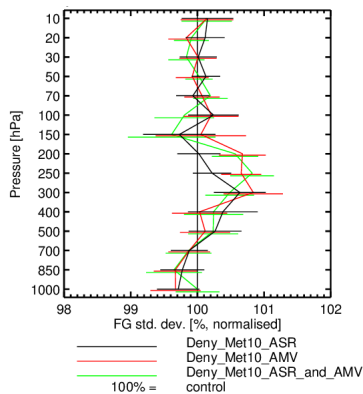
A series of experiments has been performed to assess the impact of Meteosat-10 in order to give an indication of the impact we would expect on the NWP system should we be without either ASRs, AMVs or both being assimilated, such as for the period from 7/2/18 to 19/2/18. The experiments have run for two months, so, for changes of this kind, statistically significant differences in medium-range skill are difficult to measure, so statistics of the first guess departures of other observation types is a useful way to assess the impact on the system. Figure 9 shows, for all three experiments, the change in analysis and first-guess fit to ATMS globally, and conventional wind observations in the tropics.

Instrument(s): NPP ATMS Tb Area(s): N.Hemis S.Hemis Tropics  
 From 00Z 1-Apr-2017 to 12Z 29-May-2017



(a) ATMS (global)

Instrument(s): AIREP AMprofiler EUprofiler JPprofiler PILOT TEMP - Uwind Vwind  
 Area(s): Tropics  
 From 00Z 1-Apr-2017 to 12Z 29-May-2017



(b) Conventional winds (tropics)

Figure 9: First guess departure statistics showing the effect of removing Meteosat-10 ASRs, AMVs and both together from the ECMWF NWP system. The fit to global ATMS observations is plotted, as well as the fit to conventional wind observations in the tropics.

Here we see that in the ATMS water vapour channels, the ASRs have the larger effect (as we would expect as the ASRs are sensitive to moisture), but the AMVs also produce a degraded fit when they are removed, and so the two observation types complement each other by this metric. In a similar manner, the first guess fit to tropical winds measured by conventional instruments shows that at around 250hPa, the AMVs have a larger impact, but the ASRs are also beneficial.

#### 1.2.4 Passive monitoring of Meteosat-11

From 13/2/18 to 19/2/19, the Meteosat-11 ASR data were ‘passively monitored’. By this we mean that the observations are allowed into the operational system in order that VarBC can calculate bias correction coefficients for the channels that are intended to be assimilated or used for cloud detection over sea. With this passive status, the observations do not contribute to the observation term of the 4D-Var cost function, but they do contribute to the VarBC term, though this will not have a significant effect on the analysis, but it does allow the predictor coefficients to be computed. The predictor coefficients are:

1. A fixed constant.
2. 1000-300hPa thickness.
3. 200-50hPa thickness.
4. Total column water vapour.

In the first cycle, if no coefficients are provided, the mode of the first guess departures is used as the fixed constant offset and the other predictors are set to zero. Figure 10 shows the first guess departure statistics for the two Meteosat-11 WV channels during this passive monitoring period. Note that in these plots, the channel indexing follows the RTTOV convention (i.e. the visible channels are not included). Therefore, the SEVIRI channel referred to in the plots as “2” indicates the  $6.2\mu\text{m}$  channel and so on.

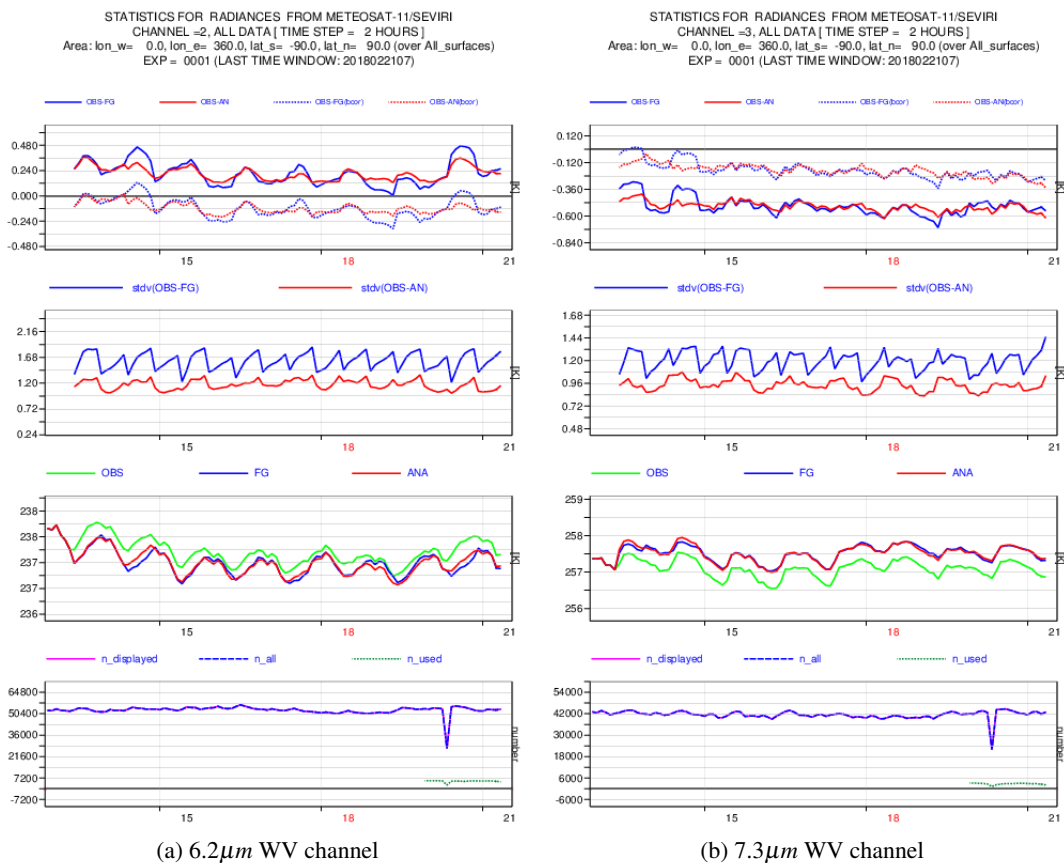


Figure 10: First guess departure statistics for Meteosat-11 ASRs for the  $6.2\mu\text{m}$  WV channel (a) and the  $7.3\mu\text{m}$  WV channel (b) on SEVIRI. Statistics of bias-corrected observations are shown with dashed lines.

It can be seen that there are biases present in the first guess departures of both channels, exceeding 0.6K. Compared to Meteosat-10, these biases are quite significantly larger which is consistent with the results shown in Letertre-Danczak [2016b] for the sample data (comparison not shown). Furthermore, the Meteosat-11 AMVs, which are derived from the radiances, exhibit a height-assignment bias which may be related to the radiance bias (Katie Lean, private communication). Importantly, however, the standard

deviations are very similar to those of *Meteosat-10*. The bias correction does remove the majority of the bias, but a residual bias does remain. It is interesting to see how the bias correction is partitioned into the four different bias correction predictor coefficients (see Figure 11).

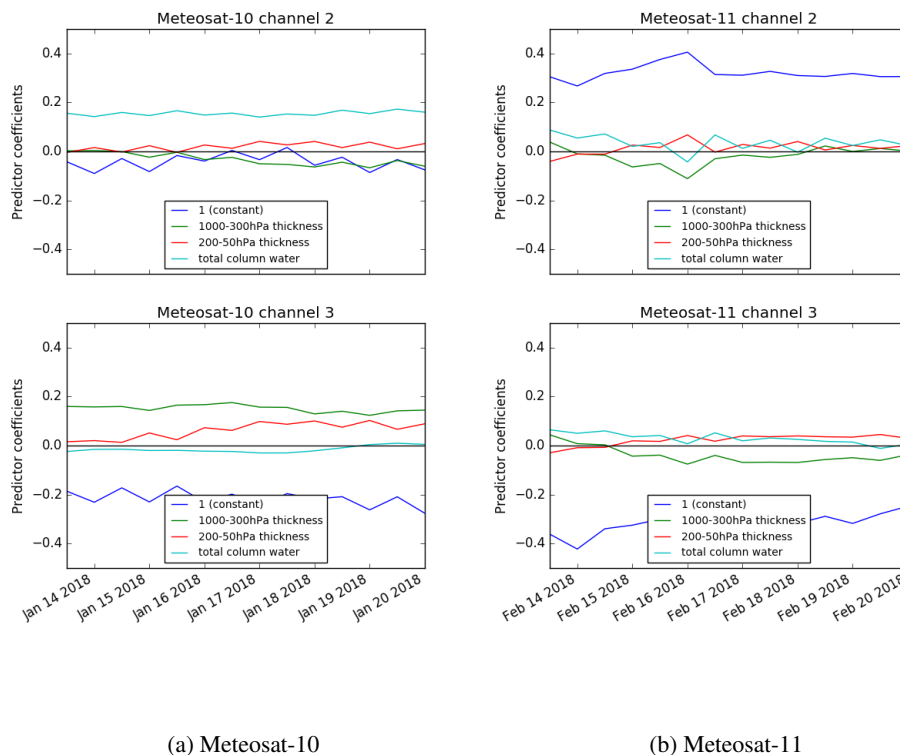


Figure 11: Time series of the bias predictor coefficients for the water vapour channels of *Meteosat-10* (a) and *Meteosat-11* (b). The *Meteosat-11* plot is from the period when the data were being passively monitored.

It can be seen that the partitioning of the coefficients is quite different for *Meteosat-10* and *Meteosat-11*. In particular, the constant offset is significantly larger for *Meteosat-11*. This is to be expected as spin-up begins, but for this period the coefficients are reasonably stable throughout. It is possible that given time, the various bias predictors will appear more like those of *Meteosat-10* (and hopefully minimise the residual biases), but if there is a systematic error in the instrument or calibration, the constant offset may persist.

### 1.2.5 Active assimilation of *Meteosat-11*

On 20/2/18, *Meteosat-11* was assimilated actively in the ECMWF system for the first time. Since then, the biases in the water vapour channels have persisted but VarBC is correcting these biases almost completely. Figure 12 shows the time series of first guess departure statistics for the subset of *Meteosat-11* ASR data that was actively assimilated. The standard deviations of the first guess departures have been fairly constant.

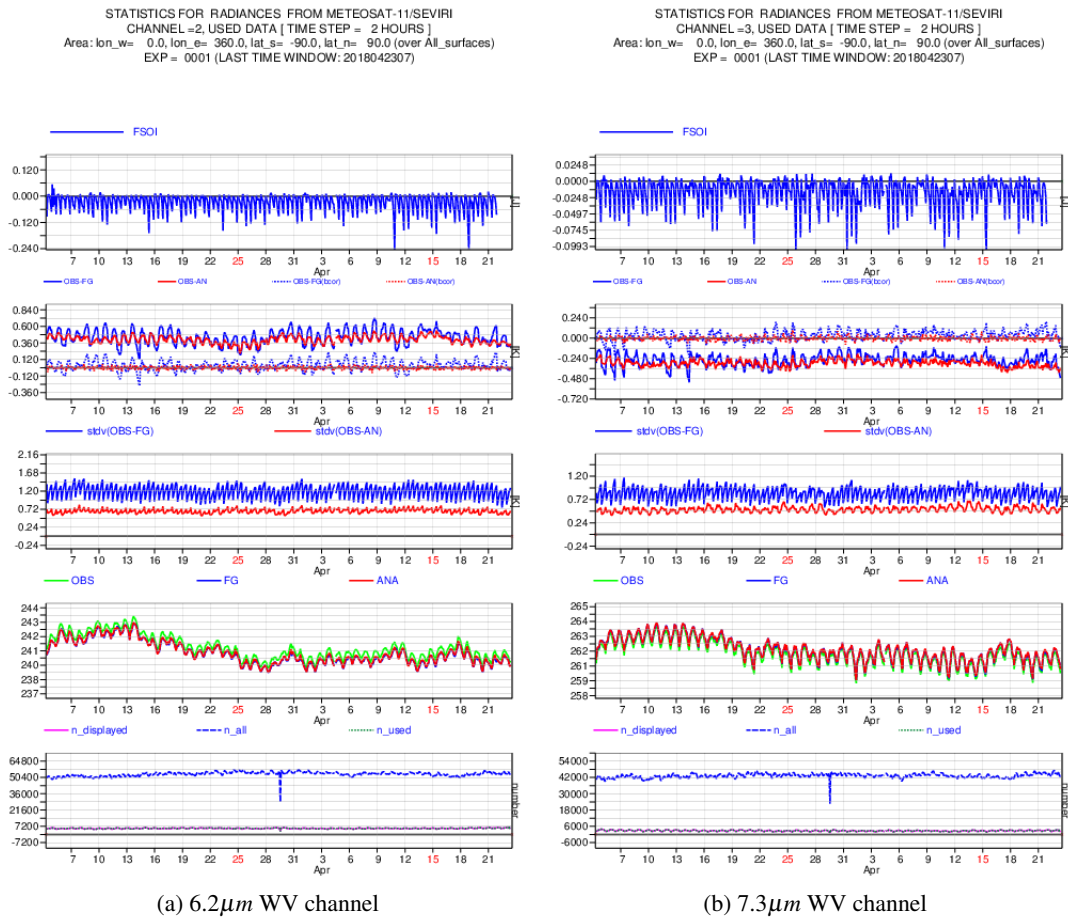


Figure 12: First guess departure statistics for Meteosat-11 ASRs for the 6.2µm WV channel (a) and the 7.3µm WV channel (b). These statistics were computed from data which were actively assimilated in the ECMWF system.

An experiment has not yet been run to assess Meteosat-11, but as it is another SEVIRI instrument, it would be reasonable to expect that the impact would be similar to that of Meteosat-10 as seen in Section 1.2.3.

### 1.3 Himawari-9 — a first look

Himawari-9 was launched on 2 November 2016, though it is not intended to become operational until 2022, when it will replace Himawari-8 and remain active until 2030. Both Himawari-8 and Himawari-9 carry the same imaging instrument, the Advanced Himawari Imager (AHI). Until 2022, Himawari-9 will remain in on-orbit storage, but will act as a backup in the event of problems with Himawari-8, and it has already produced replacement imagery in the case of planned maintenance activities. Some CSR test data, were prepared by JMA in 2017, covering the period 8-14 March 2017. The CSR products from this period were made available via ftp, and a monitoring experiment was set up to produce first guess departures for this satellite in order to compare them with those from Himawari-8, which has been assimilated since 2016 and produced positive impact (Letertre-Danczak [2016a]). The two satellites have very similar orbital positions, so it is possible to perform a reasonable comparison. Although the

analysed data from the two satellites are from a very similar period, there are slight differences in the data counts between the two satellites at the start and end of the chosen period.

The analysis here is restricted to the three WV channels, and the window channel that would be used for additional cloud checks over ocean. Note that the experiment performed here is fully passive, so VarBC predictor coefficients are not produced for Himawari-9. Himawari-8 is assimilated actively in the experiment. Figure 13 shows geographic plots of counts, mean first guess departures and standard deviations of first guess departures for the  $6.25\mu m$  WV channel on Himawari-8 and Himawari-9. Figures 14, 15 and 16 show equivalent plots for the  $6.95\mu m$  WV channel, the  $7.35\mu m$  WV channel and the  $10.45\mu m$  window channel respectively. These statistics were generated using all observations supplied in the BUFR files, with no quality control applied. The analysis given here is not intended to be rigorous, but should provide an indication of the quality we can expect from Himawari-9 with a view to assimilating it in the future.

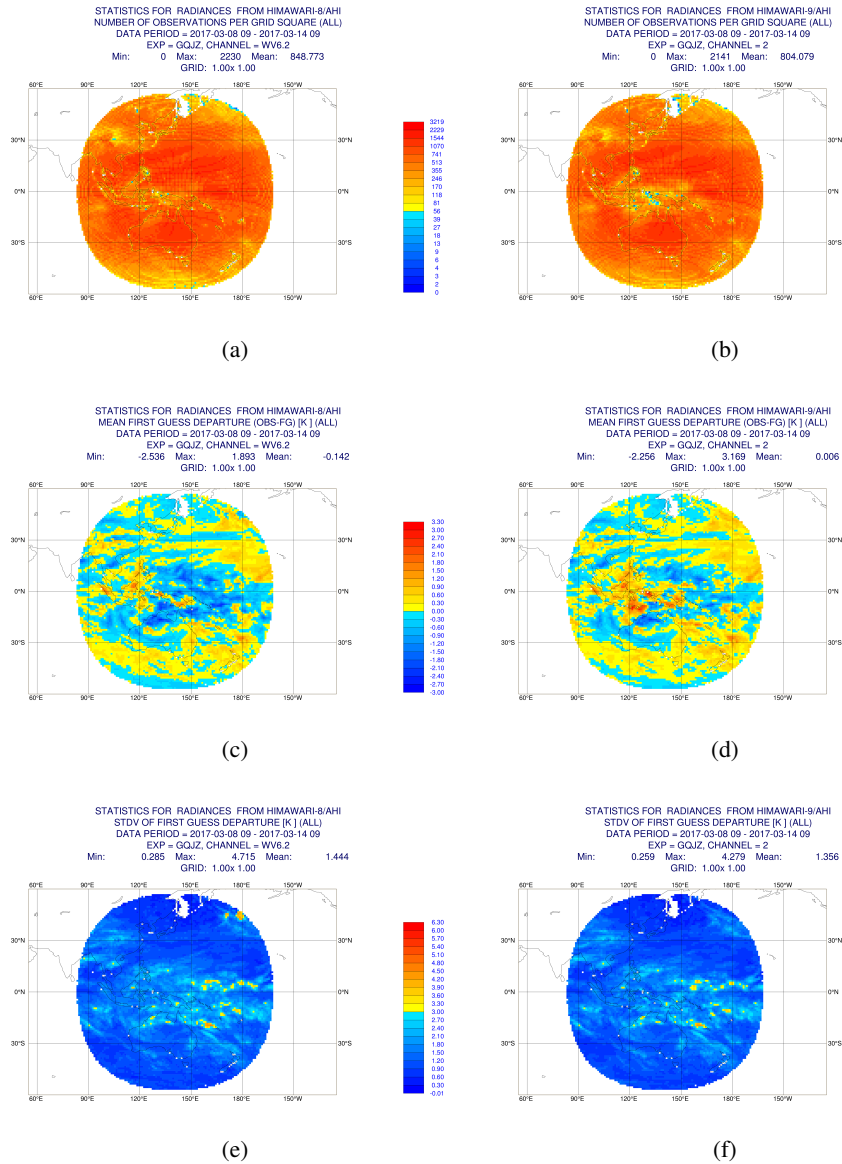


Figure 13: CSR first guess departure statistics for the  $6.25\mu\text{m}$  WV channel on Himawari-8 (left) and Himawari-9 (right). Plotted are counts (a and b), mean of first guess departures (c and d) and standard deviation of first guess departures (e and f).

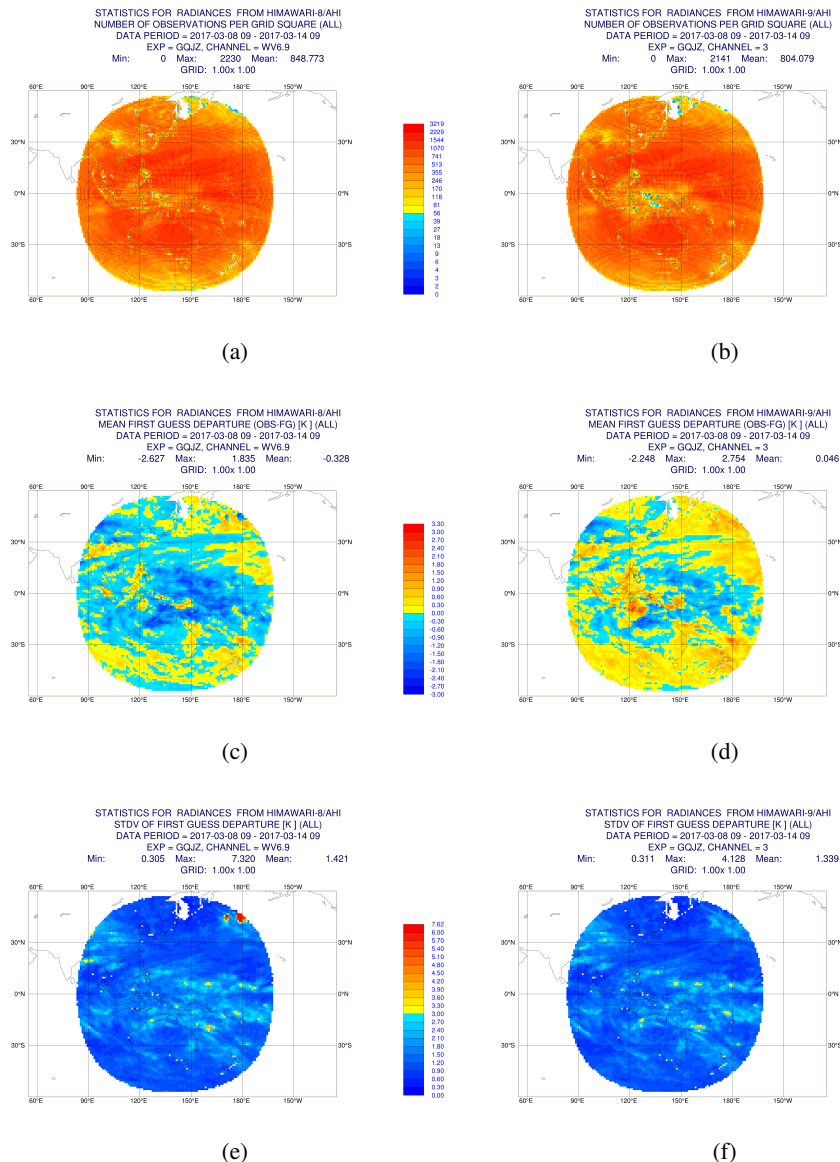


Figure 14: CSR first guess departure statistics for the  $6.95\mu\text{m}$  WV channel on Himawari-8 (left) and Himawari-9 (right). Plotted are counts (a and b), mean of first guess departures (c and d) and standard deviation of first guess departures (e and f).

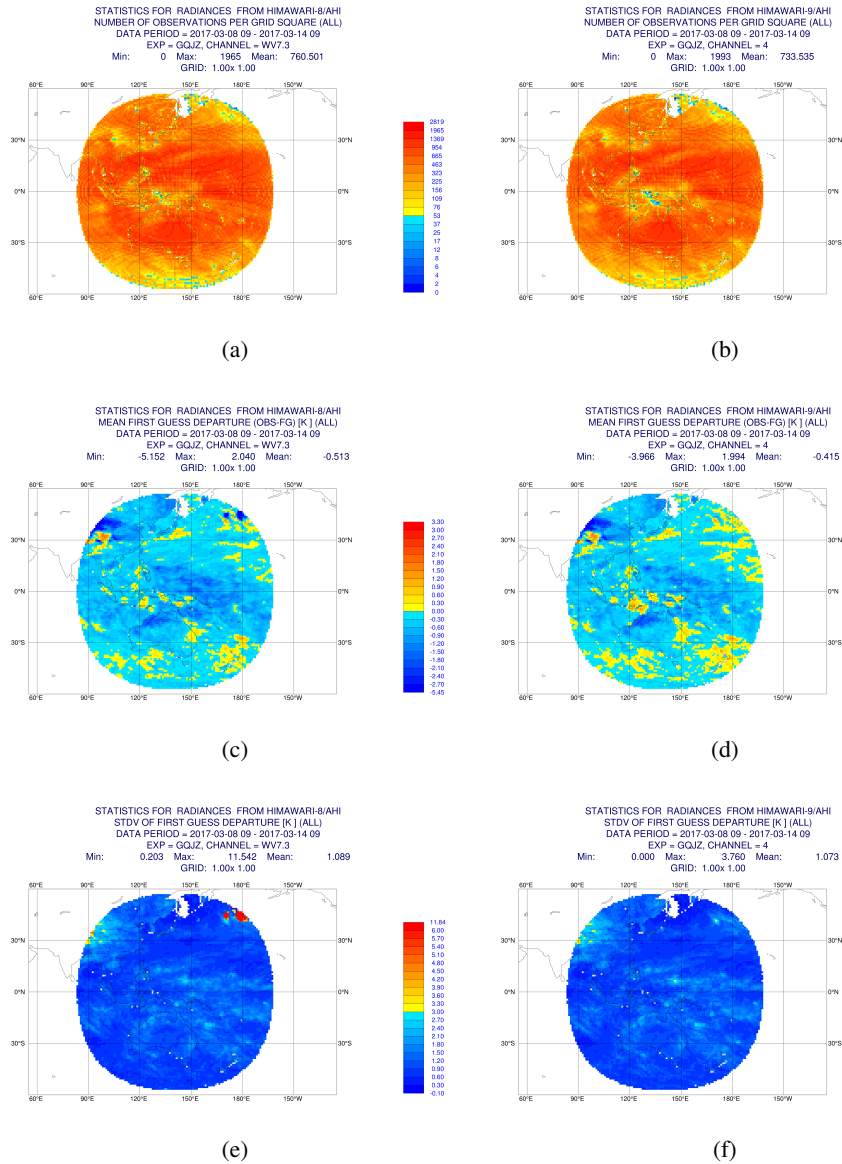


Figure 15: CSR first guess departure statistics for the  $7.35\mu\text{m}$  WV channel on Himawari-8 (left) and Himawari-9 (right). Plotted are counts (a and b), mean of first guess departures (c and d) and standard deviation of first guess departures (e and f).

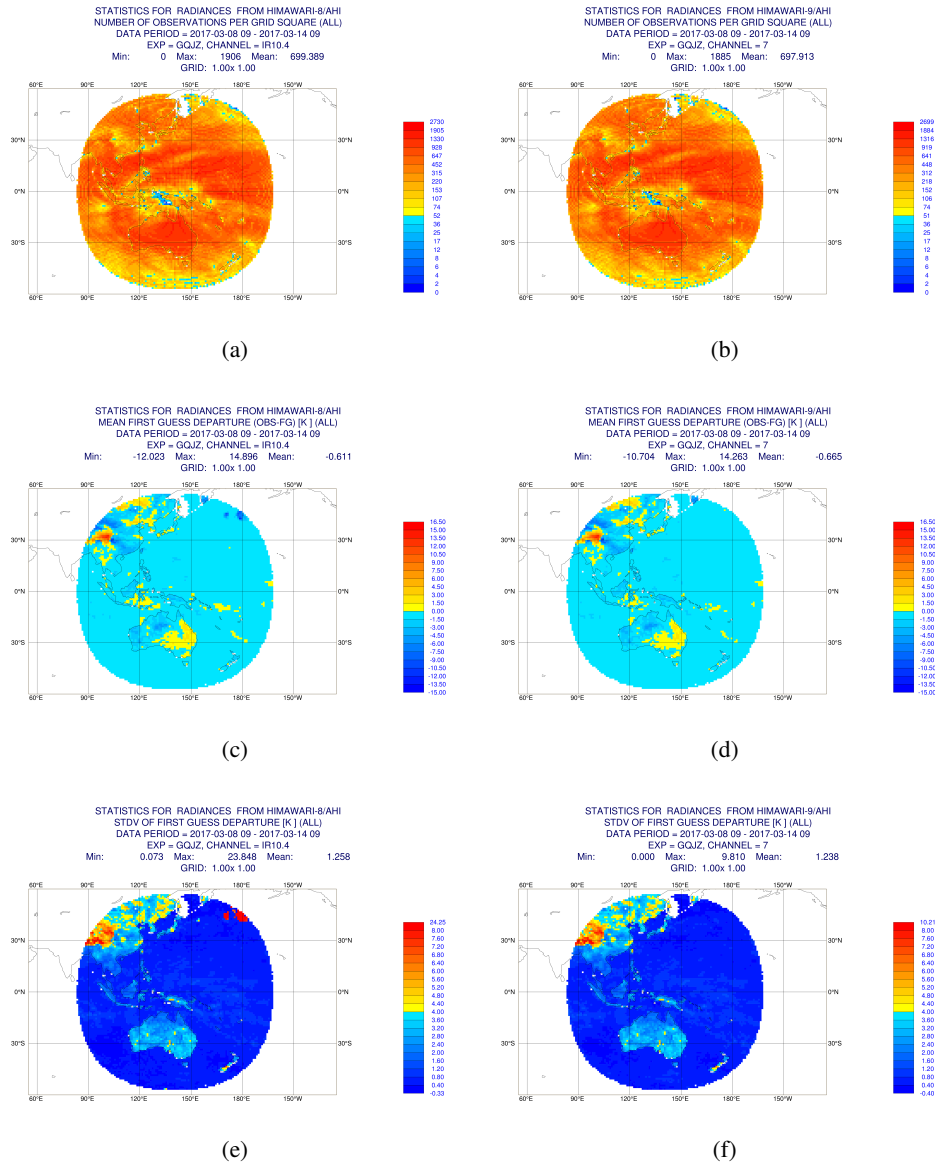


Figure 16: CSR first guess departure statistics for the  $10.45\mu\text{m}$  window channel on Himawari-8 (left) and Himawari-9 (right). Plotted are counts (a and b), mean of first guess departures (c and d) and standard deviation of first guess departures (e and f).

It can be seen that there is broad qualitative agreement between Himawari-8 and Himawari-9, but some differences do exist. For example, Himawari-9 provides fewer observations at nadir (i.e. at the centre of the disc). There is also a localised difference present in all three channels; in the north-east of the disc there is an area showing large negative first guess departures in the Himawari-8 data, and this is not present for Himawari-9. This is likely to be a cloud effect, but the origin of this difference has not yet been investigated further, though it is known that the same algorithm was used to generate CSRs for the two satellites (Yusuke Ioka, private communication). Generally, the standard deviations of the first guess departures for the water vapour channels are very similar for Himawari-8 and Himawari-9, which would be an important consideration if we were planning to assimilate these data. The means of the first guess departures are, however, slightly different, particularly for the  $6.95\mu\text{m}$  channel, where there is a

systematic difference between the satellites. Generally, for data assimilation, small systematic biases can be accepted because VarBC can often correct the biases almost completely, with reference to the first guess fields. It is likely that the difference in the  $6.95\mu\text{m}$  channel is related to differences in the spectral response function (see Figure 17), although the RTTOV coefficients have been computed independently for both Himawari-8 and Himawari-9. A comparison of the humidity Jacobians for this channel (not presented here) shows only very small differences between the two satellites. Interestingly, for this channel, JMA reports (Yusuke Ioka, private communication) that the mean first guess departure for the  $6.95\mu\text{m}$  channel on Himawari-8 is 1.07K and on Himawari-9 it is 1.29K, but compared to ECMWF first guesses, the respective values for the two satellites are -0.328K and 0.046K, so the Himawari-9 observations better match the forward-modelled radiances from the ECMWF model than the Himawari-8 observations do.

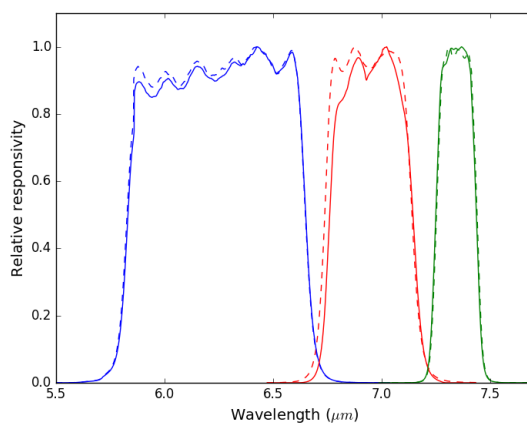


Figure 17: Spectral response functions of the three AHI water vapour channels, for Himawari-8 (dashed) and Himawari-9 (solid). The channel centred at  $6.95\mu\text{m}$  exhibits the largest differences between the two satellites. Data are from [http://www.data.jma.go.jp/mscweb/en/operation/calibration\\_portal.html](http://www.data.jma.go.jp/mscweb/en/operation/calibration_portal.html).

#### 1.4 GOES-16 (the new GOES-EAST)

GOES-R was launched in November 2016, and carries the Advanced Baseline Imager (ABI), an instrument almost identical to AHI on Himawari-8 and Himawari-9, thus providing three tropospheric WV-sounding channels. In orbit, the satellite assumed the name GOES-16, and this became the operational GOES-EAST satellite on 18 December 2017, thus replacing GOES-13. GOES-13 continued to provide data until January 2018, but was then decommissioned (see Section 1.1). Although GOES-16 has become the operational GOES-EAST satellite, the provision of CSR and ASR data was not part of the mission plans, and regrettably, the official date for operational dissemination of CSR data is currently May 2019, thus, at the time of writing, there is a gap in the coverage of assimilated geostationary data due to this delay (see Figure 2). Despite this, the team at NOAA STAR has made recent progress in the development of CSR and ASR products for GOES-16, and BUFR files containing these products are currently available via ftp for testing. These files are unofficial and the processing algorithms are subject to change, but an assessment has been performed on the data, and an assimilation experiment has been started using the CSR data (these results will not be shown due to the short period for which the data have been available).

It is difficult to produce a like-for-like comparison between GOES-16 and another satellite, because the satellites with which it produces co-located observations have slightly different channels, so such a comparison has not been attempted here.

The CSR product is encoded in BUFR format, and is very similar to the version used for Himawari and MSG, but new additions are the satellite azimuth angle (important for slant path processing, see Section 2.2) and the solar azimuth. As with other CSR data, each box-averaged brightness temperature is provided with a value that indicates the percentage of clear pixels that contributed to the average. Unlike other sources of CSR data, the initial GOES-16 data that has been analysed here was provided only if the percentage of clear pixels (“PClear”) was at least 65%, but since 19 April 2018, this threshold has been reduced to 10%. In the initial testing, the same parameters were used for GOES-16 as are used for Himawari-8 (i.e. observation errors, thinning box sizes, quality control thresholds, etc.), and this means that over land, we would reject any observations if the percentage of clear pixels was less than 50%, so one potential source of disparity between the assimilation of the two instruments could arise from the lack of GOES-16 CSR data with PClear between 50% and 65%. Moreover, observations over sea are not screened by PClear, so fewer observations will be available over ocean due to this. One slight technical difference was present in the GOES-16 BUFR compared to Himawari-8, and that is that data from two additional channels are present at the start of the files, so this has been accounted for in the source code that reads the BUFR files. The ASR files have been examined briefly, and the notable feature is that for each averaging box, only three brightness temperature values are provided; the total value, the average of the clear pixels and the average of the cloudy pixels. In addition to these, SEVIRI ASR BUFR files contain averages for low, middle and high cloud separately.

A new opportunity that has arisen with the provision of GOES-16 data is that CSR (and ASR) BUFR files are provided that contain data from full-disc scans every 15 minutes. This level of temporal resolution is a very significant improvement compared to the previous GOES data and other CSR/ASR sources. This temporal frequency of data can, in theory, provide useful information to the assimilation system through the intrinsic mechanism by which the 4D-Var system is able to track the movement of water vapour features throughout the assimilation window, and apportion these motions into wind increments (Peubey and McNally [2009]). This is especially important for geostationary radiances as, unlike data from polar-orbiters, the same geographic location can be sampled frequently, and at a full range of local solar times, which cannot be achieved with a small number of sun-synchronous polar-orbiting satellites. As a comparison, GOES-15 provides full-disc CSR data every 3 hours, plus northern hemisphere scans every hour between the full disc scans. The question of whether additional value to NWP could be gained by increasing the temporal frequency of the observations was investigated by Peubey and McNally [2009], but the study did not extend to data of this frequency, as such data were not available. In reality, a limiting factor of the usage of the data at ECMWF could be the technical issue of which model fields are matched to observations at a given time. Currently this is achieved by using ‘timeslots’; these are 30-minute bins in which the observations from within each bin are associated with a model field from a single timestep. Therefore, each observation is placed in the timeslot which has the nearest time, and so this association may introduce a time error (an error of representation) of up to 15 minutes, thus limiting the potential benefit that may be accrued from observations with high temporal resolution. In practice, the thinning algorithm will prioritise observations that are closer to the analysis time. Planned upgrades to the ECMWF system may allow the full temporal information to be extracted from these observations (Elias Holm and Peter Lean, private communication). Although no work has yet been done on this, it is a topic which is due to be pursued 3.

The assessment of the GOES-16 observations was performed by producing similar plots to those that were shown for Himawari-9 above (using the same colour scales). Recall that for this period, GOES-16

CSR data was not provided if PClear was less than 65%, so in the map plots, we may expect to see differences due to this (i.e. by construction, the GOES-16 data set contains fewer of the observations that we would otherwise be more likely to reject as part of the pre-assimilation observation screening procedure). Figure 18 shows the first guess departure statistics for the  $6.15\mu\text{m}$  and  $7.00\mu\text{m}$  WV channels on GOES-16, with all provided observations contributing to the statistics. Figure 19 shows the same set of statistics but for the  $7.40\mu\text{m}$  WV channel and the  $10.3\mu\text{m}$  window channel.

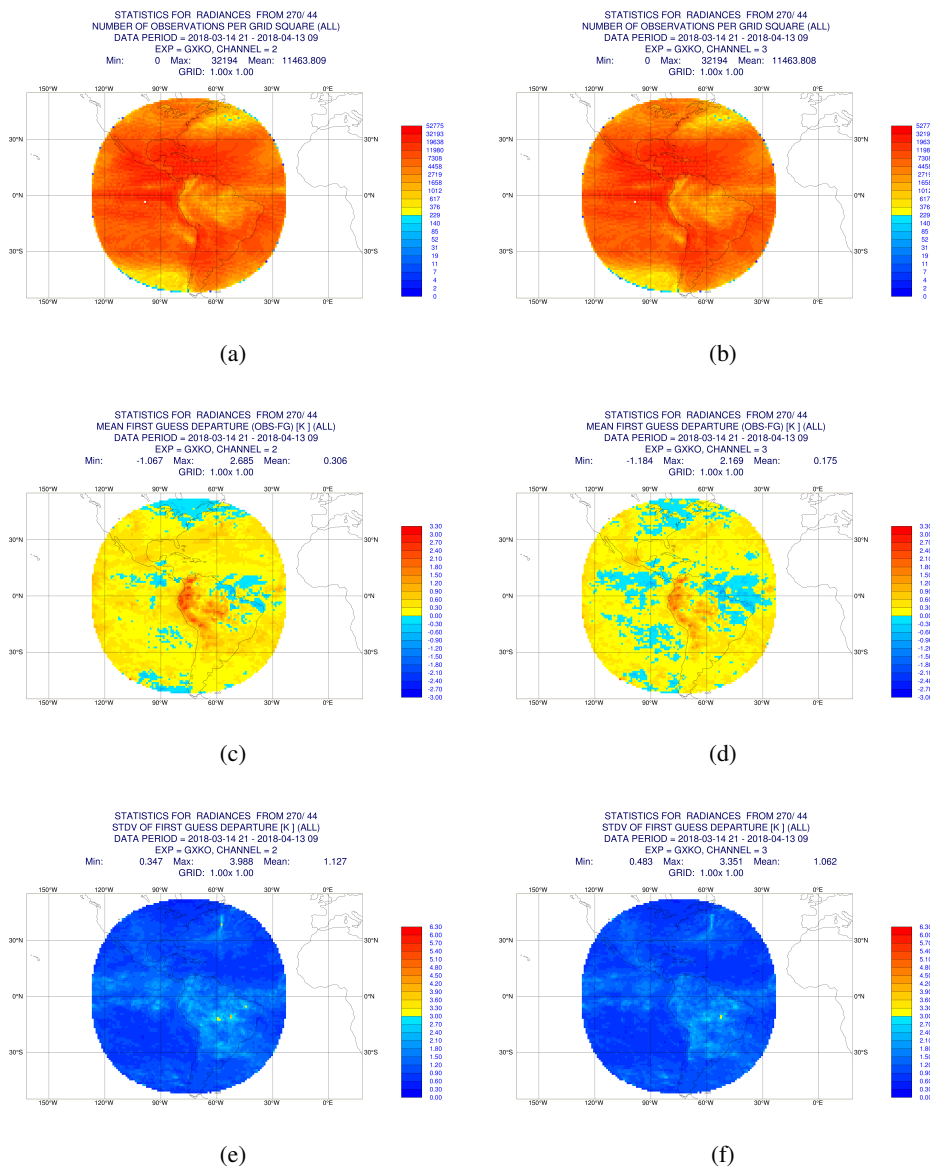


Figure 18: CSR first guess departure statistics for the  $6.15\mu\text{m}$  (left) and  $7.00\mu\text{m}$  (right) WV channels from GOES-16. Plotted are counts (a and b), mean of first guess departures (c and d) and standard deviation of first guess departures (e and f). Statistics are based on all data provided in the BUFR files.

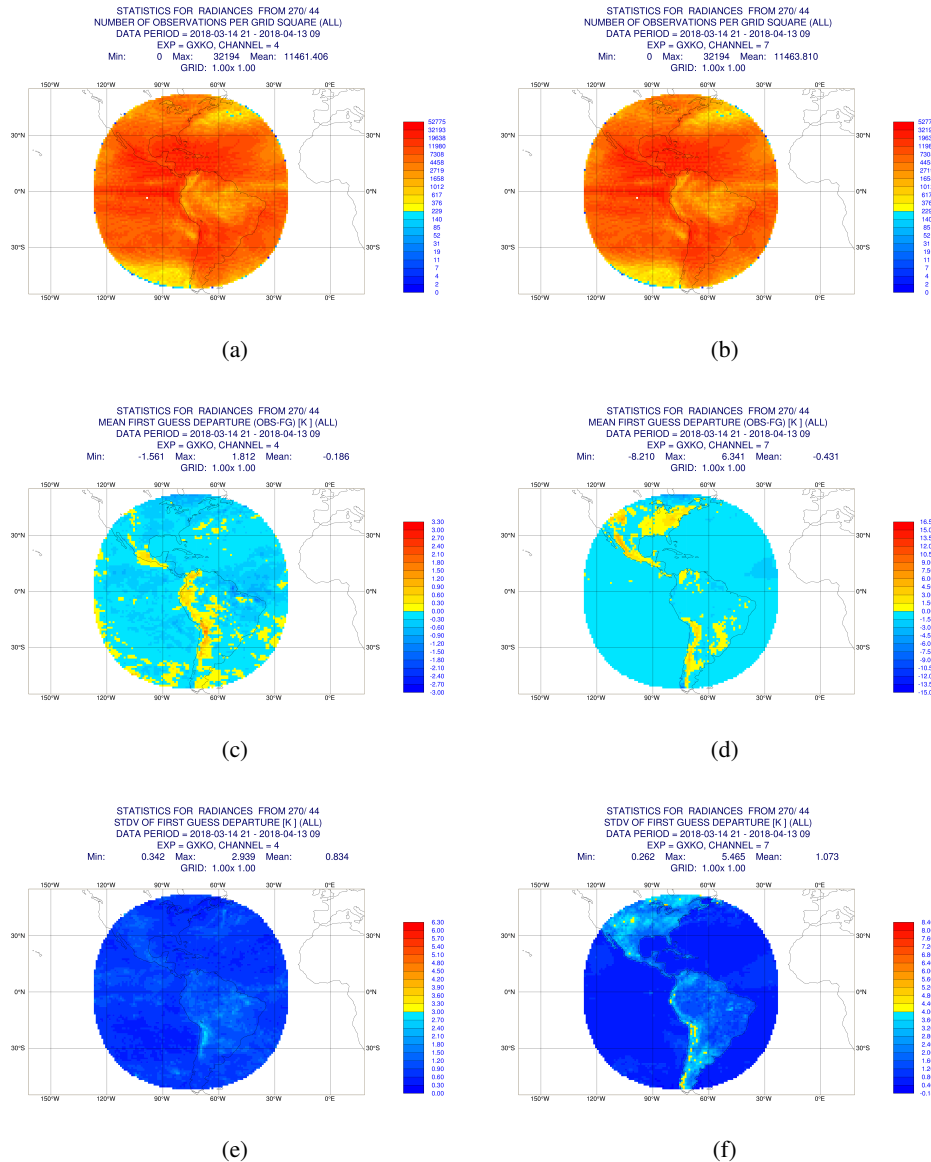


Figure 19: CSR first guess departure statistics for the 7.40µm WV channel (left) and 10.3µm window channel (right) from GOES-16. Plotted are counts (a and b), mean of first guess departures (c and d) and standard deviation of first guess departures (e and f). Statistics are based on all data provided in the BUFR files.

These plots can be compared to those of Himawari-8 and Himawari-9 (Figures 13 to 16), but with the caveat that the GOES-16 data contain no brightness temperatures for which PClear is less than 65%. The standard deviations of the first guess departures of the WV channels appear to be broadly smaller than those for Himawari-8. The standard deviations of the first guess departures of the window channel seem larger for GOES-16, but this is mostly over land, where the data are not used, but the values are slightly increased over ocean as well. The means of the first guess departures display small biases that seem fairly uniform across the disc but with a particularly large signal over South America where there is high orography. The WV-channel biases are improved considerably with VarBC. This can be seen in Figure 20 which compares the mean first guess departures of the ‘used’, i.e. assimilated, data from GOES-16

and Himawari-8, with the observations having been bias-corrected (here, the GOES-16 observations are being assimilated in an offline experiment). Figure 21 shows the same comparison but for the standard deviations of the first guess departures.

From the plots above, it appears that the cloud screening has been performed conservatively and hence, there is no sign of the large negative bias signals we would expect if the CSR product contained significant amounts of undetected cloud.

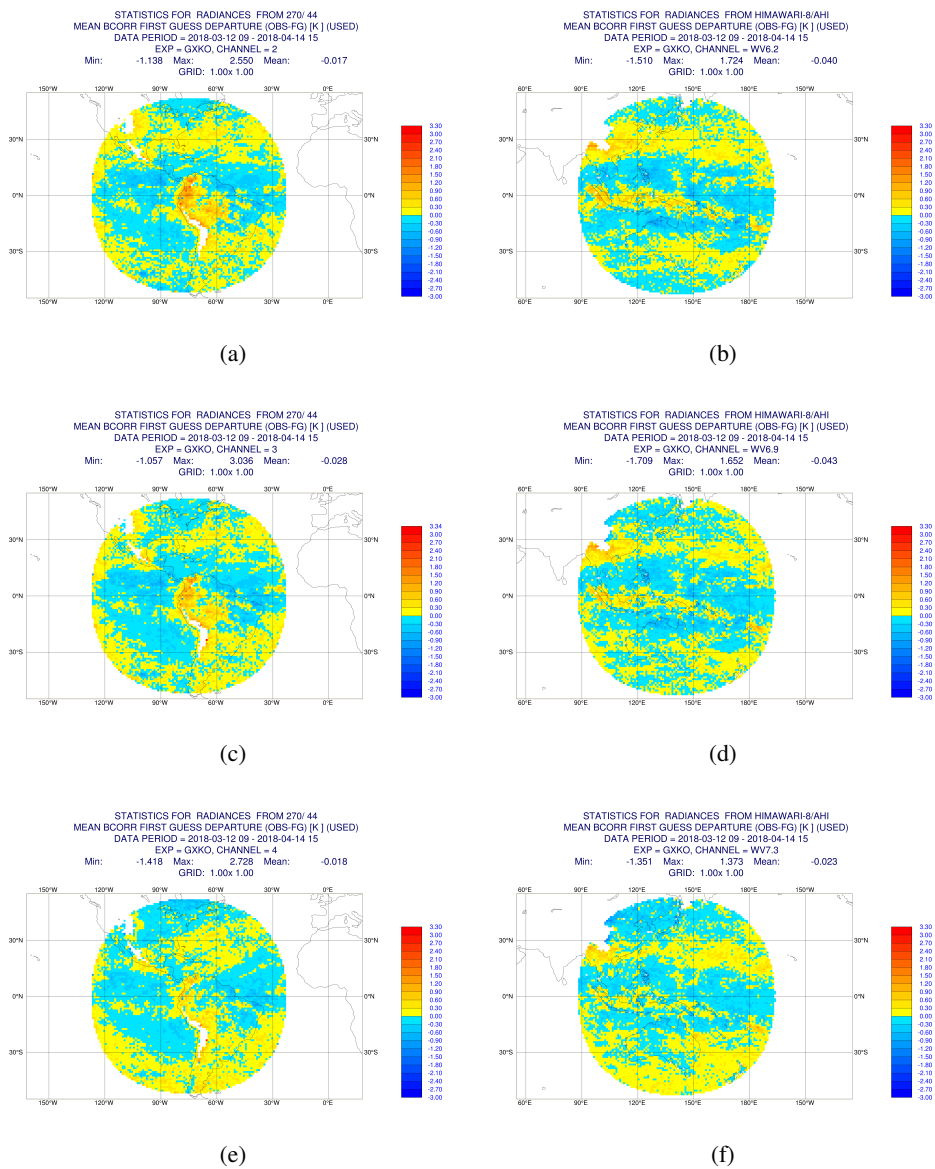


Figure 20: CSR mean first guess departures for the  $6.15\mu\text{m}$  (top),  $7.00\mu\text{m}$  (middle) and  $7.40\mu\text{m}$  (bottom) WV channels from GOES-16 (left) and Himawari-8 (right). Statistics are based on observations that were assimilated (i.e. after observation screening, quality control etc.).

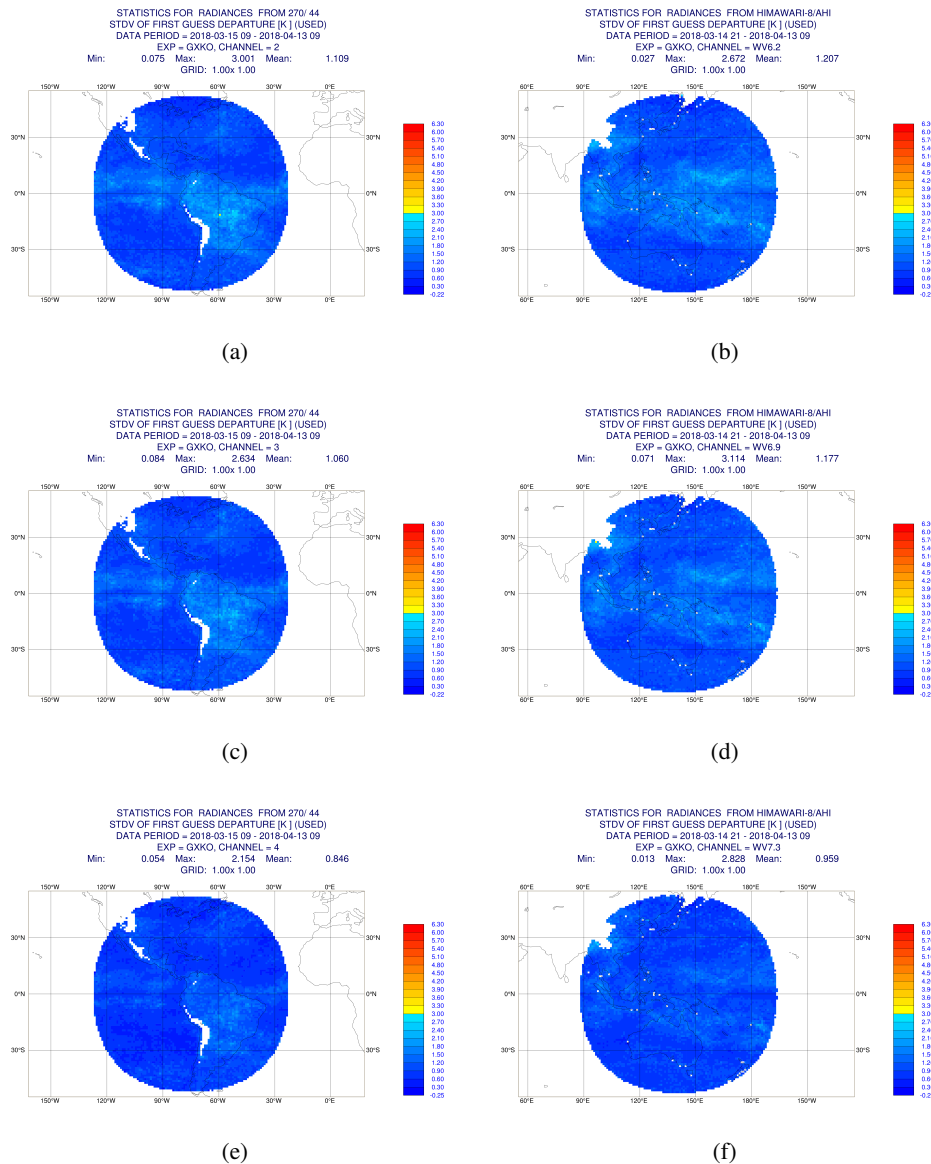


Figure 21: CSR standard deviation of first guess departures for the 6.15  $\mu\text{m}$  (top), 7.00  $\mu\text{m}$  (middle) and 7.40  $\mu\text{m}$  (bottom) WV channels from GOES-16 (left) and Himawari-8 (right). Statistics are based on observations that were assimilated (i.e. after observation screening, quality control etc.).

The bias characteristics of the three water vapour channels after the bias corrections have been applied are very similar between GOES-16 and Himawari-8, indicating that VarBC is working well at removing biases in both, and that the residual biases in the GOES-16 CSRs are not likely to be prohibitive. The most significant region of residual bias is over the northernmost part of the Andes, and it is more significant for higher-peaking channels. A similar signal is seen in the region of the Tibetan Plateau that is at the edge of the Himawari-8 disc. If this were simply related to the influence of the surface on the observations, it might be expected that the lower peaking channels would show the largest effect in the statistics. It could, however, be related to the model, if a moist bias exists in the upper tropospheric humidity field above high orography, though the exact reason for this is yet to be understood.

The standard deviations of the first guess departures are similar to Himawari-8 but slightly smaller, which may be expected as the “used” Himawari-8 data includes data from averaging boxes that contain fewer cloud-free pixels, which are intrinsically noisier.

## 2 Research to maximise the impact of geostationary radiance data when assimilated

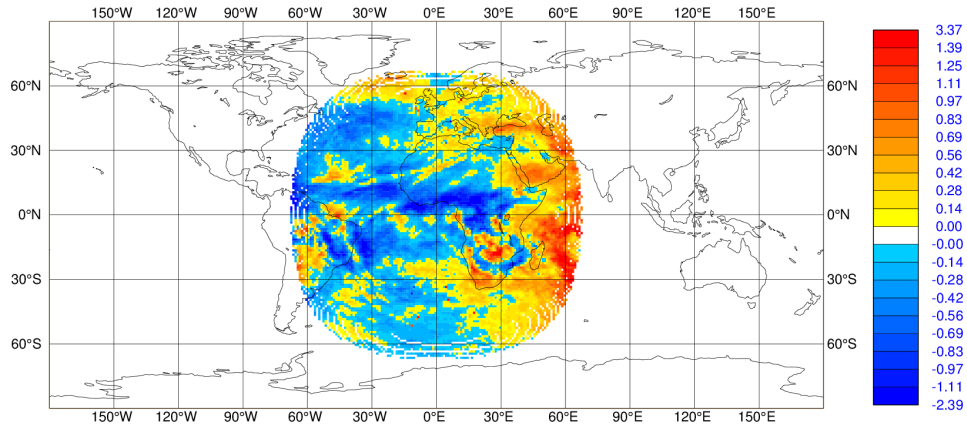
### 2.1 Effect of spacecraft position and orbit on SEVIRI CSRs

When assessing Meteosat-11 during the transition from Meteosat-10, it was discovered that during the drift, there existed a clear east-west bias structure in geographical plots of the mean of the first guess departure statistics. As noted in the previous section, there was no period during which the two satellites were at the same nominal longitude, so an exact like-for-like comparison is difficult. Figure 22 shows geographic plots of the mean first guess departures of the  $6.2\mu\text{m}$  WV on both Meteosat-10 and Meteosat-11. The observations that contributed to the statistics were from 31/1/18 to 14/2/18, including periods when both satellites were drifting. Meteosat-10 was drifting from  $0^\circ$  toward the east, and Meteosat-11 was drifting to  $0^\circ$  from the west.

In Section 1.2 it was noted that there was a net bias difference between the first guess departures of the equivalent WV channels on Meteosat-10 and Meteosat-11, and this can be seen in Figure 22, hence demonstrating that the observations from Meteosat-11  $6.2\mu\text{m}$  channel are systematically warmer than those from Meteosat-10. As well as this difference, there is a superposed east-west bias present in each plot, but it can be seen that the sign of the bias is opposite between Meteosat-10 and Meteosat-11. This east-west bias would appear to be correlated with the longitude of the sub-satellite point; if the satellite is east of  $0^\circ$  (i.e. Meteosat-10), the observations east of  $0^\circ$  have a positive bias and those to the west have a negative bias (and vice versa for Meteosat-11 which is west of  $0^\circ$ ). Physically, there is no reason for such an east-west bias to be present in the measured radiances, nor in the first guess fields, if the radiative transfer is computed correctly. Importantly, each brightness temperature observation is provided with the satellite zenith angle in the BUFR file, thus allowing the radiative transfer calculations to be modified to account for the oblique path through the atmosphere (for geostationary radiances this is currently done by scaling the layer thicknesses of a single interpolated model column, but Section 2.2 discusses progress towards accounting for the slant path radiative transfer more correctly). So, it is possible that this bias characteristic may be related to some aspect of the low-level observation processing.

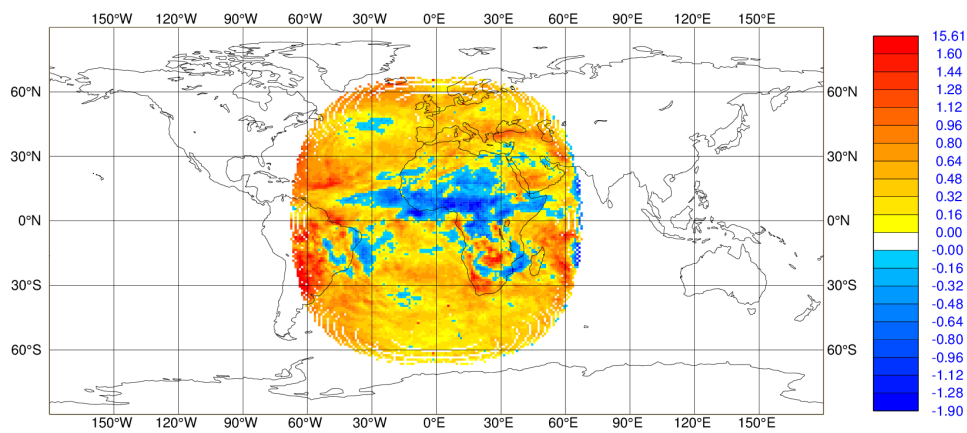
The ASR products are based on Level-1.5 images, which are derived from the Level-1 data, and have undergone radiometric and geometric corrections (EUMETSAT [2015, 2017]). Notably, this processing step involves the transformation of the raw images to appear as if the satellite was above  $0^\circ$  for the  $0^\circ$  Full Disc Service and at  $41.5^\circ E$  for the Indian Ocean Data Coverage (IODC) service. To attempt to ascertain whether the source of the bias is due to the Level-1.5 data, simultaneous images from Meteosat-10 and Meteosat-11 were obtained for comparison (thanks to Crispian Batstone, Met Office). These images are from the  $6.2\mu\text{m}$  WV channel and are valid for 12Z on 9/2/18 (Figure 23). This was a unique date because Meteosat-10 was at  $1.5^\circ E$  and Meteosat-11 was at  $1.5^\circ W$ , thus equidistant from the rectification centre (i.e.  $0^\circ$ ).

STATISTICS FOR RADIANCES FROM METEOSAT-10/SEVIRI  
 MEAN FIRST GUESS DEPARTURE (OBS-FG) (ALL)  
 DATA PERIOD = 2018-01-31 21 - 2018-02-14 21  
 EXP = GVYX, CHANNEL = WV6.2  
 Min: -2.248 Max: 3.227 Mean: -0.077  
 GRID: 1.00x 1.00



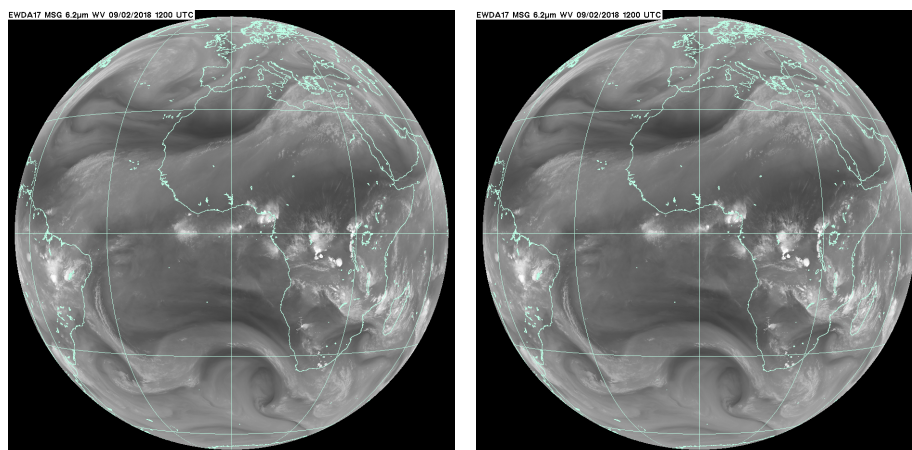
(a) Meteosat-10: Sub-satellite longitude: 0.9°E – 4.0°E

STATISTICS FOR RADIANCES FROM METEOSAT-11/SEVIRI  
 MEAN FIRST GUESS DEPARTURE (OBS-FG) (ALL)  
 DATA PERIOD = 2018-01-31 21 - 2018-02-14 21  
 EXP = GVYX, CHANNEL = 2  
 Min: -1.740 Max: 15.455 Mean: 0.267  
 GRID: 1.00x 1.00



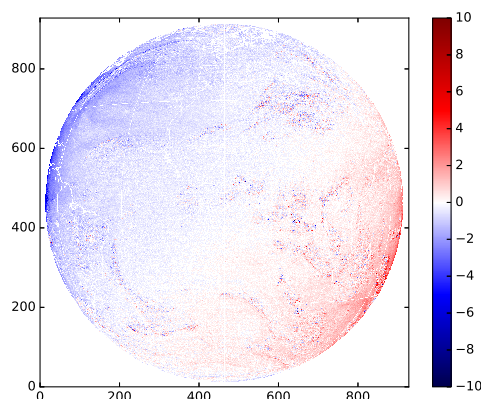
(b) Meteosat-11: Sub-satellite longitude: 3.5°W – 0.0°W

Figure 22: Mean of the first guess departures of the 6.2μm WV channel on Meteosat-10 (a) and Meteosat-11 (b) during the period when the two satellites were drifting.



(a) Sub-satellite longitude: 1.5E

(b) Sub-satellite longitude: 1.5°W



(c) Brightness temperature difference (Met11-Met10).

Figure 23: Reduced-resolution level-1.5 images from the  $6.2\mu m$  WV channel on Meteosat-10 (a) and Meteosat-11 (b) during the period when the two satellites were drifting (12Z on 9/2/18). The images have been rectified to appear as if the sub-satellite point is at  $0^\circ N, 0^\circ E$ . The absolute difference of the brightness temperature between the two satellites is also shown (c).

It is difficult to see differences between the images from Meteosat-10 and Meteosat-11 by eye, but discernible differences are present. When the brightness temperature difference is plotted (Figure 23c), it is clear that there is a bias pattern very roughly in the east-west direction. This would appear to be consistent with the bias characteristics in Figure 22, though the axis of negative mirror symmetry in Figure 23c is rotated somewhat from the north-south direction. Pursuing the line that the bias pattern is related to the rectification step from the true sub-satellite point to  $0^\circ N, 0^\circ E$ , we can look at the latitude of the sub-satellite points to determine more accurately the axis along which the rectification has been applied. On 9/2/18, when the images were obtained, the orbital inclinations of Meteosat-10 and Meteosat-11 were  $0.87^\circ$  and  $1.43^\circ$  respectively. From this, and other information available from EUMETSAT (<https://www.eumetsat.int/website/home/Data/ServiceStatus/MeteosatOrbitalParameters/index.html>), the sub-satellite point at a given time can be calculated (Arthur de Smet, private communication). This al-

allows us to determine the directions in which the observations have been transformed — this is shown graphically in Figure 24.

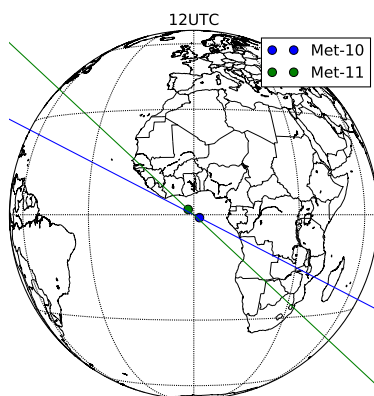


Figure 24: The sub-satellite positions of Meteosat-10 and Meteosat-11 at 12Z on 9/2/18. Also shown are the directions in which the rectification of the data from each satellite has been performed in the Level-1.5 processing.

The rectification directions are approximately consistent with the brightness temperature differences shown in Figure 23c. This comparison is only valid for one moment, and the north-south diurnal variation of the sub-satellite point would result in a cancellation of any north-south biases when statistics are accumulated over 24 hours, which is consistent with Figure 22.

If this bias is due to the rectification, it would be expected that the error should scale with the magnitude of the distance from the true sub-satellite point to the centre of rectification. Currently, Meteosat-8 has a particularly large orbital inclination since the north-south station-keeping manoeuvres ceased in 2010. Since then, the inclination has grown larger monotonically, and it is currently over  $5^\circ$  (see Figure 25a). This means that diurnally, the sub-satellite point oscillates in the north-south direction with an amplitude of  $\sim 5^\circ$  in geocentric latitude. Figure 25 also shows the subset of *used* (i.e. assimilated) data for Meteosat-8 at 00Z and 12Z on a particular day in February 2017. The disc is seen to move significantly in the north-south direction. The reason for this is that observations with satellite zenith angles greater than  $60^\circ$  are not currently assimilated, and the zenith angles provided in the BUFR files are those of the true satellite positions, hence the sub-disc of assimilated data is centred on the true sub-satellite position. Note also that there are fewer assimilated observations in the western part of the disc; this is due to the thinning procedure, where Meteosat-8 and Meteosat-10 (at this time) were being thinned together where they overlap.

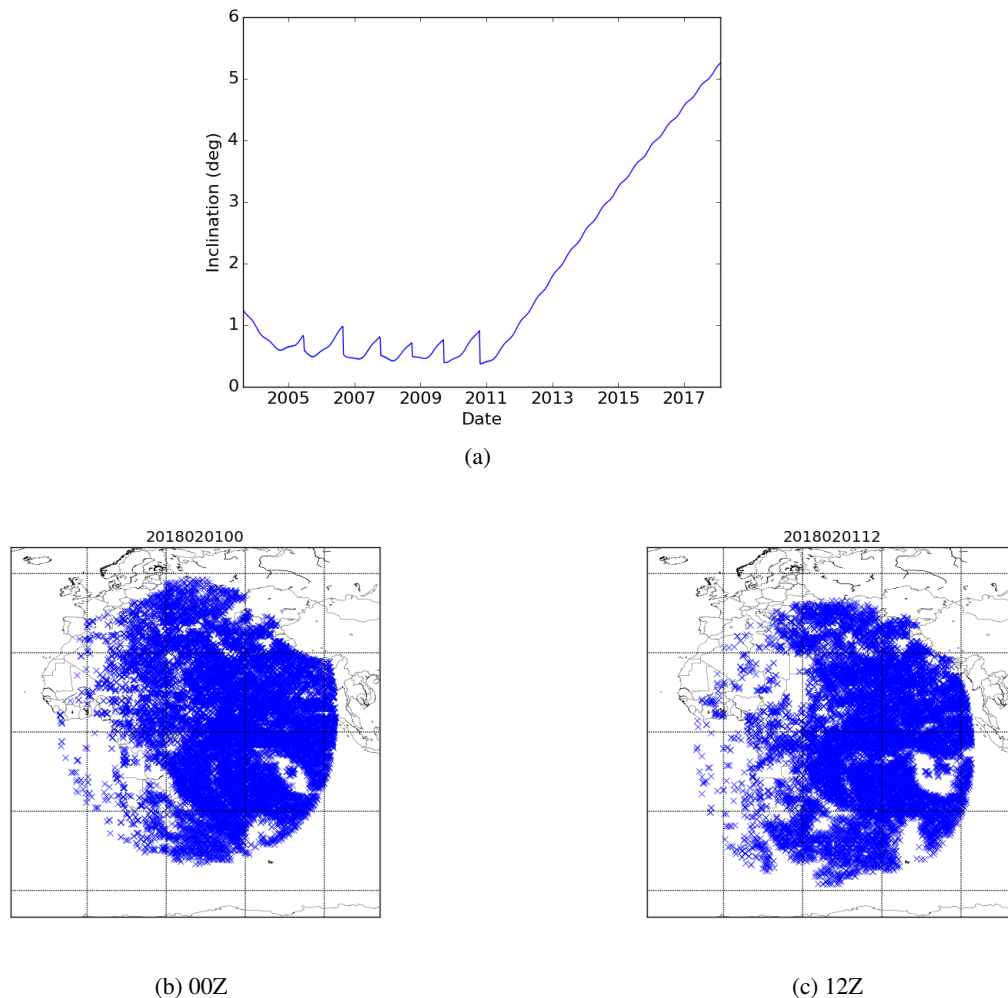


Figure 25: Time series of the orbital inclination of Meteosat-8 (a), and the subset of assimilated data at 00Z (b) and 12Z (c) on 1/2/18, showing the truncated disc centred on the true sub-satellite point.

Although the true sub-satellite position is used in the computation of the satellite zenith angles, the experience from the Meteosat-10/11 transition has shown that systematic differences appear to exist along the rectification direction, so it may be expected that similar differences are present in the diurnal variation of Meteosat-8, but in the north-south direction.

The equator crossing time of Meteosat-8 varies continually. In fact, the UTC time at which the satellite reaches its most northerly position regresses by approximately two hours per month, see Figure 26.

In order to assess any potential bias between the north and south parts of the Meteosat-8 orbit, geographic plots need to be produced for the northernmost and southernmost extremes of the orbit. Based on Figure 26, for the period of 1 February 2018 to 1 April 2018, statistics were accumulated from 19Z to 21Z to sample the northernmost part of the orbit, and 07Z to 09Z to sample the southernmost part. The means of the first guess departures for these two windows are shown in Figure 27 for the  $6.25\mu\text{m}$  WV channel and Figure 28 for the  $7.35\mu\text{m}$  WV channel, for both raw and bias-corrected observations.

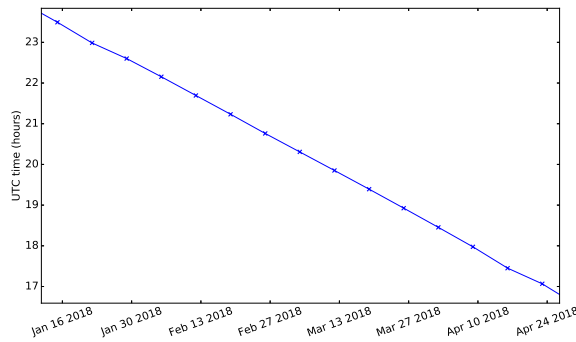


Figure 26: The UTC time at which Meteosat-8 reached its most northerly position in early 2018.

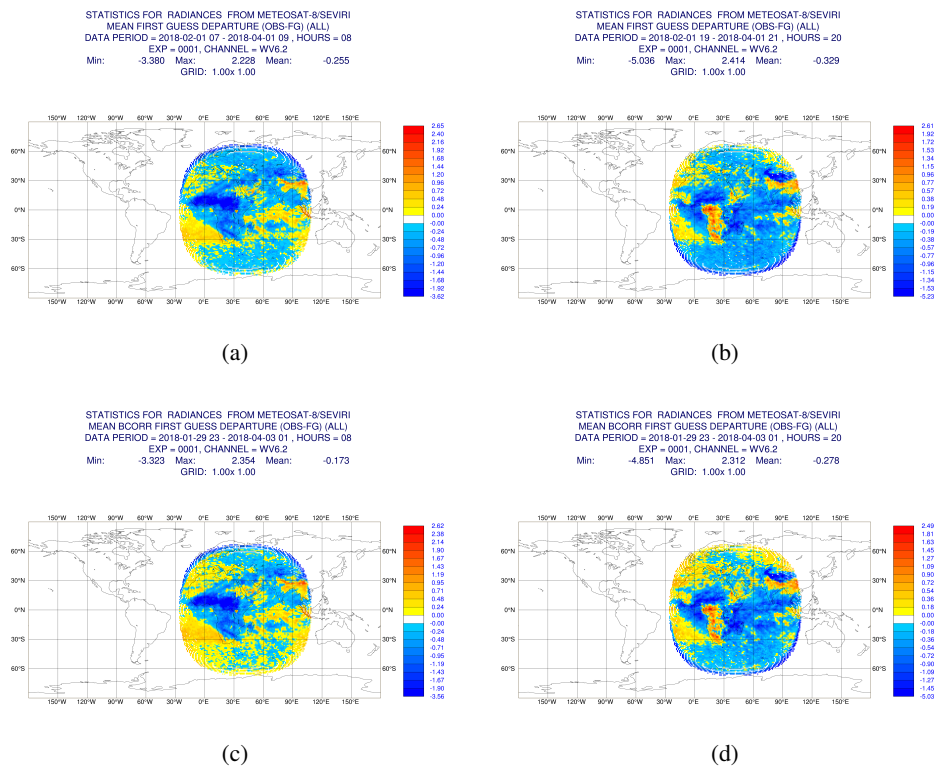


Figure 27: Mean first guess departures for the  $6.25\mu\text{m}$  WV channel from Meteosat-8 before (top) and after (bottom) bias correction. The left-hand plots include statistics from 07Z to 09Z (when the satellite was at the most southerly part of its orbit for this period) and the right-hand plots include statistics from 19Z to 21Z when the satellite was at its most northerly extent.

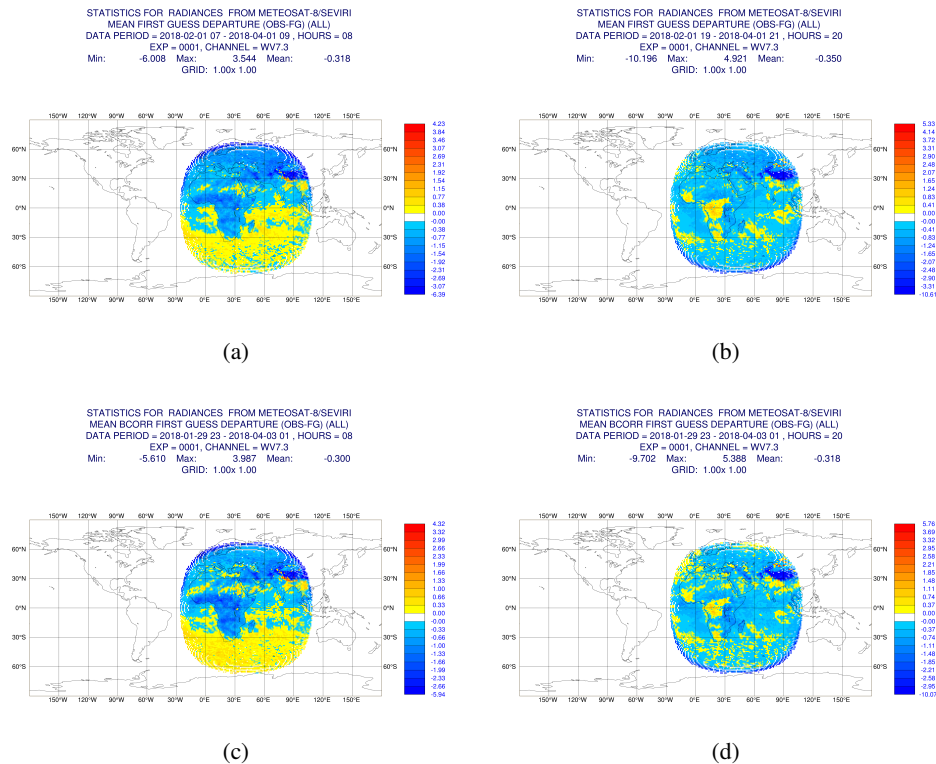


Figure 28: Mean first guess departures for the 7.35 μm WV channel from Meteosat-8 before (top) and after (bottom) bias correction. The left-hand plots include statistics from 07Z to 09Z (when the satellite was at the most southerly part of its orbit for this period) and the right-hand plots include statistics from 19Z to 21Z when the satellite was at its most northerly extent.

The 6.25 μm channel of Meteosat-8 (Figure 27) shows a clear north-south bias pattern whose sign depends on whether the satellite is at the northern or southern part of its orbit, and this seems to be consistent with the relation between the bias and the spacecraft position highlighted in Figure 22. The pattern is even more pronounced when the bias correction has been applied. The 7.35 μm channel (Figure 28) shows a similar pattern that is particularly striking when the satellite is at its most southerly extent, but at its most northerly point, the pattern is much less pronounced, except for a large negative bias at the southern edge of the disc. A comparison with Meteosat-11 (results not presented) has shown that the north-south pattern does not exist, thus indicating that the Meteosat-8 bias is due to the satellite’s position relative to the rectification centre and not a different diurnal factor specific to the measurements or the first guess fields.

This topic of investigation has not been pursued further, but clearly, in order to maximise the impact of the radiances, the removal of systematic biases is desirable, whether this is done by updating processing algorithms or by introducing appropriate bias predictors to account for these biases at the assimilation stage.

## 2.2 Assimilation of geostationary radiance data at high zenith angles with slant path radiative transfer

If a geostationary radiance observation is measured with a satellite zenith angle of more than  $60^\circ$ , it is rejected from the assimilation. This restriction was originally implemented due to limitations within RTTOV (Munro et al. [2004]). Currently, warnings are produced by RTTOV if the zenith angle is larger than  $75^\circ$ , so the purpose of this section is to assess whether we can make use of data with larger zenith angles. Figure 29 shows concentric rings of constant zenith angle for the example of a Meteosat satellite over the prime  $0^\circ$  longitude position. The shaded area indicates the data we currently reject, but could possibly make use of.

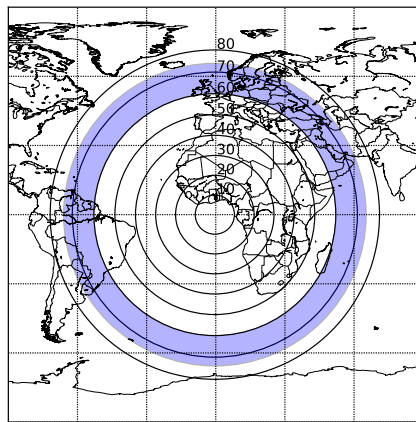


Figure 29: Lines of constant zenith angle for a geostationary satellite at  $\text{lat}=0^\circ$ ,  $\text{lon}=0^\circ$ . The blue shaded region indicates the data that would currently be discarded but which RTTOV could process in principle.

The maximum additional geographic coverage provided by relaxing this threshold can be calculated for a single satellite:

$$A_{\text{before}} = \int_0^\circ \int_0^\circ r^2 \sin \theta d\theta d\phi = 1.27 \times 10^{14} m^2$$

$$A_{\text{after}} = \int_0^\circ \int_0^\circ r^2 \sin \theta d\theta d\phi = 1.85 \times 10^{14} m^2$$

This is an increase in surface area of a factor of approximately 1.4. Of course, some of this additional coverage would overlap with the discs of other satellites, and some satellites do not provide data to  $74^\circ$ , but additional overall coverage would be obtained at the northern and southernmost parts of the geostationary coverage. An indication of this can be inferred from Figure 2.

The observations are provided with latitude and longitude values that describe a point on the Earth's surface, and during the assimilation process, an interpolated vertical model profile centred at this position

is used to perform the radiative transfer calculations. For observations close to nadir, this is perfectly representative, but for observations with large zenith angles, the true line-of-sight to the satellite is poorly described by this vertical approximation, particularly if the observations are sensitive to features high in the atmosphere. In order to minimise this source of error, the “slant-path” can be accounted for in the radiative transfer calculation, by tracing a straight line path from the point on the surface of the Earth to the satellite and interpolating model columns to this path in order to best represent the true path of radiation received by the instrument. This was implemented in the IFS system for polar-orbiting satellites (Bormann et al. [2007], Bormann [2016]) so, in order to extend this to work for geostationary radiances, only minimal additions were required. The main addition required was that the BUFR files for the geostationary radiances do not include the satellite azimuth angle, which is required in order to know which direction the satellite is in for a given observation location. Unfortunately, the files do not contain sufficient metadata to compute this accurately, but by assuming a fixed sub-satellite point, the azimuth can be calculated to a good approximation. Figure 30 shows an example of computed azimuth angles for a geostationary satellite at  $0^\circ$  latitude,  $0^\circ$  longitude. Also shown is the error introduced by assuming that the satellite is at  $0^\circ$  lat,  $0^\circ$  lon when it is really at  $5^\circ$  lat,  $0^\circ$  lon. The magnitude of this error would be consistent with the maximum extent of the north-south diurnal variation in the position of Meteosat-8 (see Section 2.1).

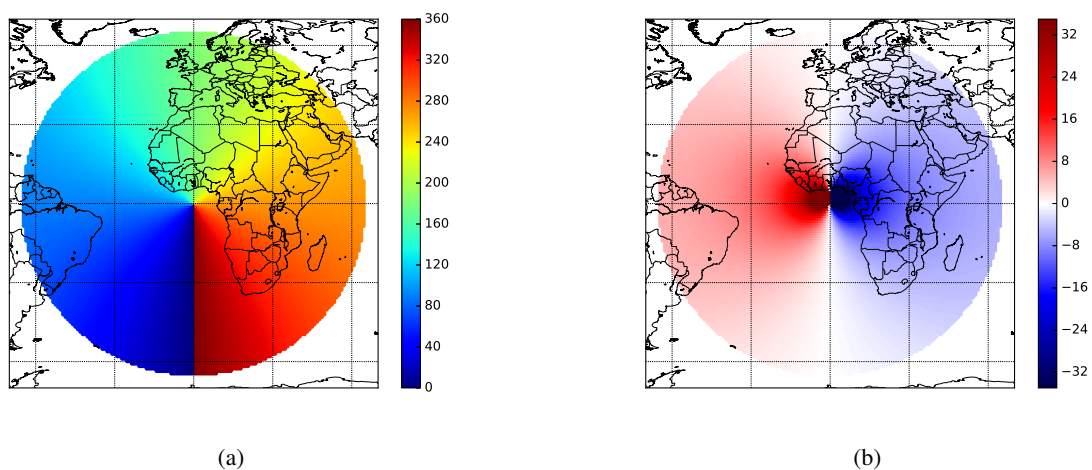


Figure 30: Computed satellite azimuth angles (degrees) for a satellite at  $0^\circ$  latitude,  $0^\circ$  longitude (a) and the error in computed azimuth angle if the true sub-satellite point is displaced to  $5^\circ$  latitude (b).

The error introduced by misplacing the nominal satellite position is largest between the true and nominal positions, where the error is  $180^\circ$ . This seems very large, but fortunately for our purposes, these locations are close enough to nadir that the zenith angle will be so small that the error in the computed azimuth is irrelevant. To the east and west of the nominal sub-satellite point there is a significant error in computed azimuth angle which decreases rapidly with distance from the nominal position. For this example, along the line  $\text{lat}=0^\circ$ , for zenith angles greater than  $20^\circ$ , the absolute azimuth error is less than  $19^\circ$  and for zenith angles greater than  $40^\circ$  the absolute azimuth error is less than  $9^\circ$ . Although a  $5^\circ$  displacement is the maximum we would currently expect from the operational satellites, these are clearly deficiencies in the calculation, but compared to neglecting the slant path altogether, this is still likely to be an improvement. In particular, the fact that the errors are largest where the zenith angle is smallest indicates that the

Name	Latitude	Longitude
Meteosat-7	0.0°	57.3°
Meteosat-8	0.0°	41.5°
Meteosat-10	0.0°	0.0°
Meteosat-11	0.0°	0.0°
GOES-13	0.0°	-75.0°
GOES-15	0.0°	-135°
GOES-16	0.0°	-75.2°
Himawari-8	0.0°	140.7°

Table 1: Nominal sub-satellite positions used for azimuth calculations.

slant-path calculation should still be relatively robust given fixed nominal sub-satellite positions.

The nominal sub-satellite positions are given in Table 1.

An assessment of the geolocation error introduced by the neglect of the slant path calculation has been performed. Note that this neglects any error in the azimuth. Consider a geostationary satellite over a point on the equator. For a measurement at the sub-satellite position (i.e. nadir), there is no need to account for the slant path, but as we consider observations at higher zenith angles, it becomes increasingly important. To keep the geometry simple, we focus here on the plane shown in Figure 31, whereby the satellite is over the equator and it measures radiation coming from the direction of a point on the north-south meridian that intersects the sub-satellite point. When assimilating radiances from WV channels, these observations are sensitive to water vapour in the troposphere, and from the geometry in the diagram it can be seen that if these features are at a height  $h$  above the surface, the satellite will, for an off-nadir observation, measure radiation which is sensitive to the atmospheric state at the point  $p_2$ . Although, unless slant-path considerations are made, the model information that would be used to compute the simulated radiance would actually come from point  $p_1$ . The distance between these points,  $dx$ , is a proxy for the spatial error of representation, and this increases with zenith angle.

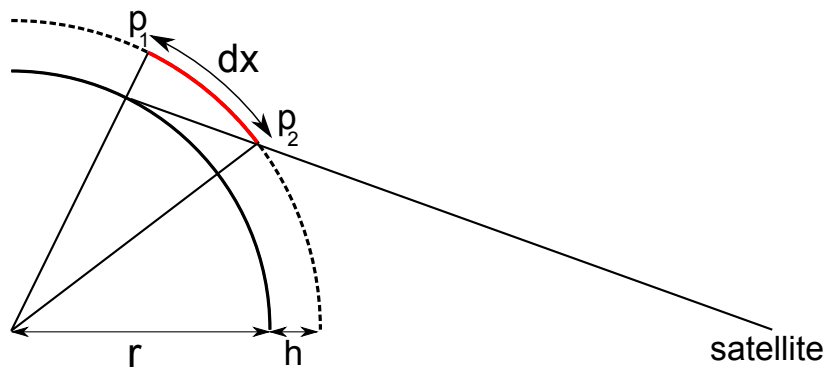


Figure 31: Diagram illustrating the spatial error of representation,  $dx$ , introduced when observing a feature at height  $h$  when slant-path processing is not performed.

Remaining with the geometry in Figure 31, we can calculate the spatial error  $dx$  produced by neglecting slant path processing as a function of the latitude north of the equator. These absolute errors have been plotted in Figure 32 for a range of heights of features. For example, for a feature at 8km<sup>1</sup>, if the

<sup>1</sup> 8km was chosen to be approximately consistent with the weighting function peaks of typical GEO WV channels.

observation is at a latitude of  $50^\circ$  on the meridian, the spatial error from neglecting the slant-path is approximately 11km, but at a latitude of  $65^\circ$  this error increases to 27km, thus indicating the importance for accounting for the slant path if the maximum zenith angle limit is increased for geostationary radiances. At the time of writing, the operational horizontal resolution of nonlinear integrations of the IFS model is approximately 10km, so, for zenith angles greater than about  $50^\circ$ , the error is greater than the model grid spacing (cf. Figure 29).

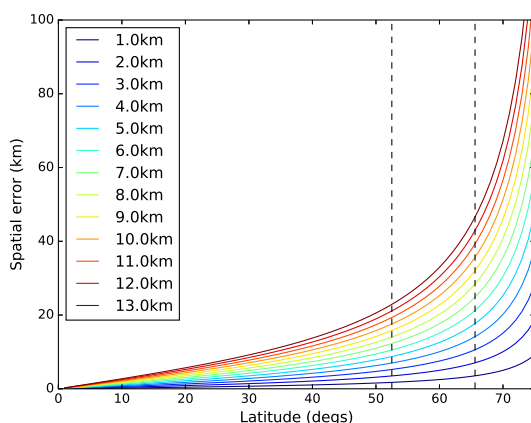


Figure 32: Absolute spatial error of representation of observations along the north-south meridian defined by the sub-satellite point that is due to the neglect of slant-path radiative transfer. These errors are plotted for features at a range of heights. The current  $60^\circ$  zenith angle limit is marked (equivalent to a latitude of  $52.5^\circ$ ), as is the proposed limit of  $74^\circ$  (equivalent to a latitude of  $65.6^\circ$ ).

Although the azimuth angle must always be calculated, the zenith angle is provided in all CSR and ASR BUFR files, though this was only a relatively recent addition for the SEVIRI ASR data, and during the period for which the slant-path processing was tested (December 2016), zenith angles were not available from Meteosat-10 (they were being provided, but not yet being extracted from the BUFR files), and so these too were calculated using the nominal sub-satellite positions in Table 1. During this period, the orbital inclination of Meteosat-10 was approximately  $0.6^\circ$ . As well as the error due to the neglect of slant-path processing, for this inclination we can also calculate the error that originates from assigning the wrong latitude of the sub-satellite point. These absolute errors are shown in Figure 33 for a feature at a height of 8km (roughly where the water vapour sensitivity is greatest for  $\sim 6.25\mu m$  channels). Note that this plot is for the northern hemisphere only. When the satellite is at the most northerly extent of its orbit, the errors are slightly reduced because the observations are closer to nadir. Conversely, when the satellite is at its most southerly position, the errors are increased slightly, as the true zenith angle is larger. Despite this, the magnitude of the spatial error caused by neglecting the slant-path radiative transfer is much larger than the small perturbation seen as a result of assuming the satellite is always above the equator.

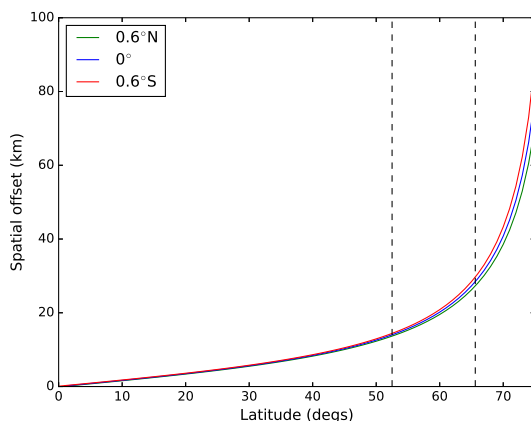


Figure 33: Absolute spatial error of representation of observations along the north-south meridian defined by the sub-satellite point that is due to the neglect of slant-path radiative transfer. This graph is valid for features at a height of 8km. Also shown are the maximum perturbations that would occur if the true zenith angle was neglected, i.e. if the sub-satellite latitude of Meteosat-10 was assumed to be  $0^\circ$ , but it was really orbiting with an inclination of  $0.6^\circ$ .

Of all the available satellites during the period of testing, Meteosat-10 provided observations up to the largest zenith angles, and so provided the best source of data for assessing the utility of data at high zenith angles, and the impact of slant-path processing. From Figure 33 we can see that for an orbital inclination as small as  $0.6^\circ$ , the calculated zenith angle for a fixed satellite position is adequately representative, so we will proceed with this process.

The first question in assessing whether to consider using observations at large zenith angles operationally is to examine the first guess departures of the water vapour channels, binned by zenith angle. These are shown in Figure 34.

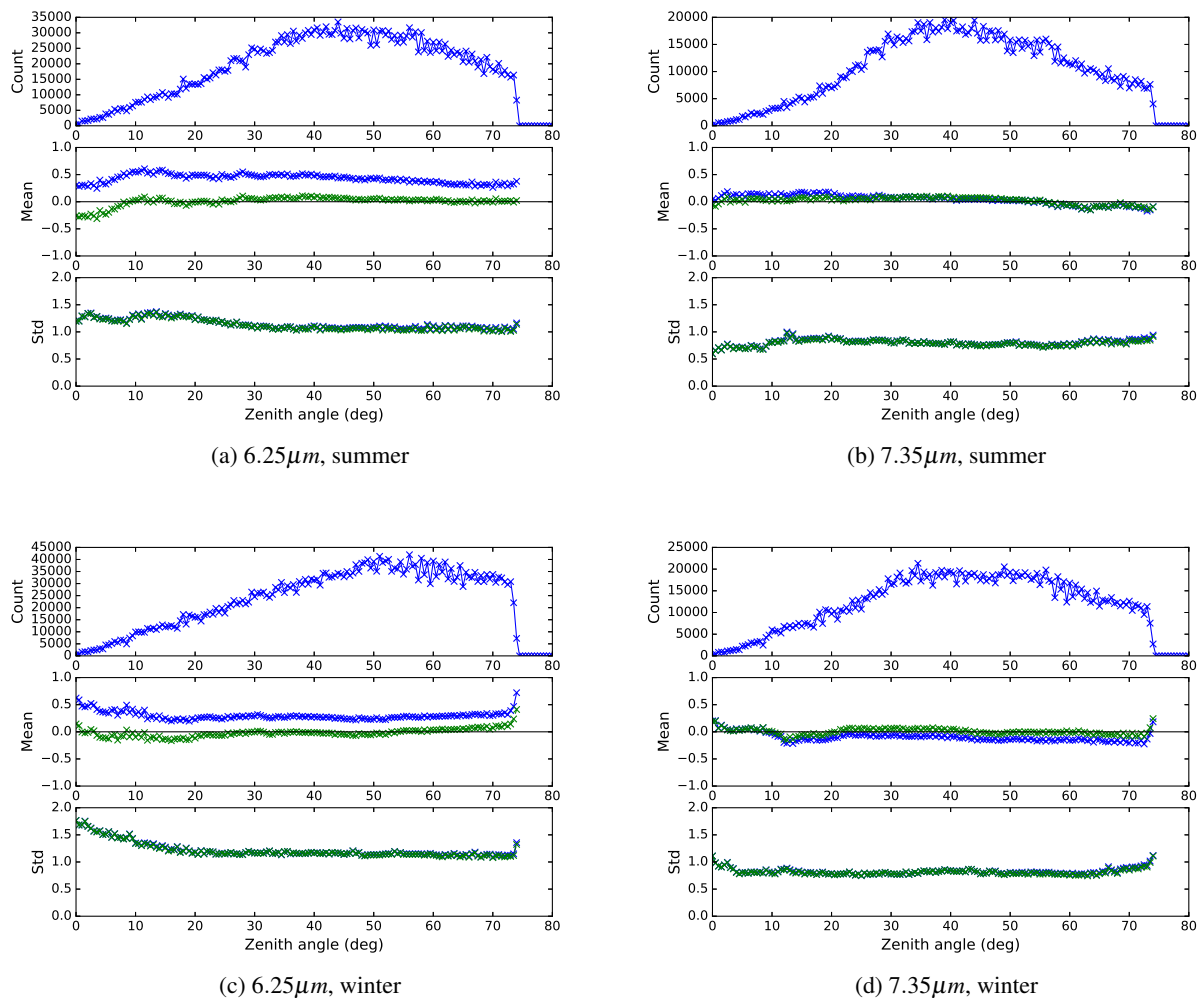


Figure 34: Meteosat-10 first guess departures of “used” data in an experiment where the zenith angle limit was increased from  $60^\circ$  to  $74^\circ$ . The first guess departures are binned by zenith angle, and are shown for the two water vapour channels, and for two seasons. The blue lines are for raw data, and the green lines are for data after bias corrections have been applied. Slant-path processing is not performed.

When assessing Figure 34, it is valuable to compare it with Figure 29 to see the areas sampled by the zenith angle binning. At small zenith angles, the relatively large standard deviations in the  $6.25\mu\text{m}$  channels are likely to be due to sampling a specific part of the disc (i.e. western Africa and the eastern Atlantic). At zenith angles above  $60^\circ$ , it is interesting to note that for the  $6.25\mu\text{m}$  channel, there is no significant variation in the standard deviations for either season, but for the  $7.35\mu\text{m}$  channel, there is a small increase in the standard deviations, particularly in winter. This is slightly surprising as the  $7.35\mu\text{m}$  channel peaks lower in the troposphere, so the error from not accounting fully for the off-nadir aspect of the radiation ought to be smaller than for the higher peaking channel. The explanation is likely to be related to the relative horizontal length scales of water vapour features at the different heights, i.e. higher in the troposphere the water vapour features are smoother in the horizontal. Regardless of this, the increase in standard deviation for large zenith angles is fairly small, so there is scope to make use of this data.

Another question is; by accounting for the slant-path, is it possible to improve the fit of the simulated observations to the measured observations? This has been assessed in another experiment. The caveat here is that the experiment is cycling, i.e. the slant-path processing of the backgrounds is used in the radiative transfer calculations, and this affects the analysis via the adjoint, and hence successive backgrounds are also modified, so the changes we see will include contributions from both the direct change in the forward-modelling and the indirect effect of the modified background fields. Figure 35 shows the differences in first guess departures due to the slant-path radiative transfer in the two channels for both seasons.

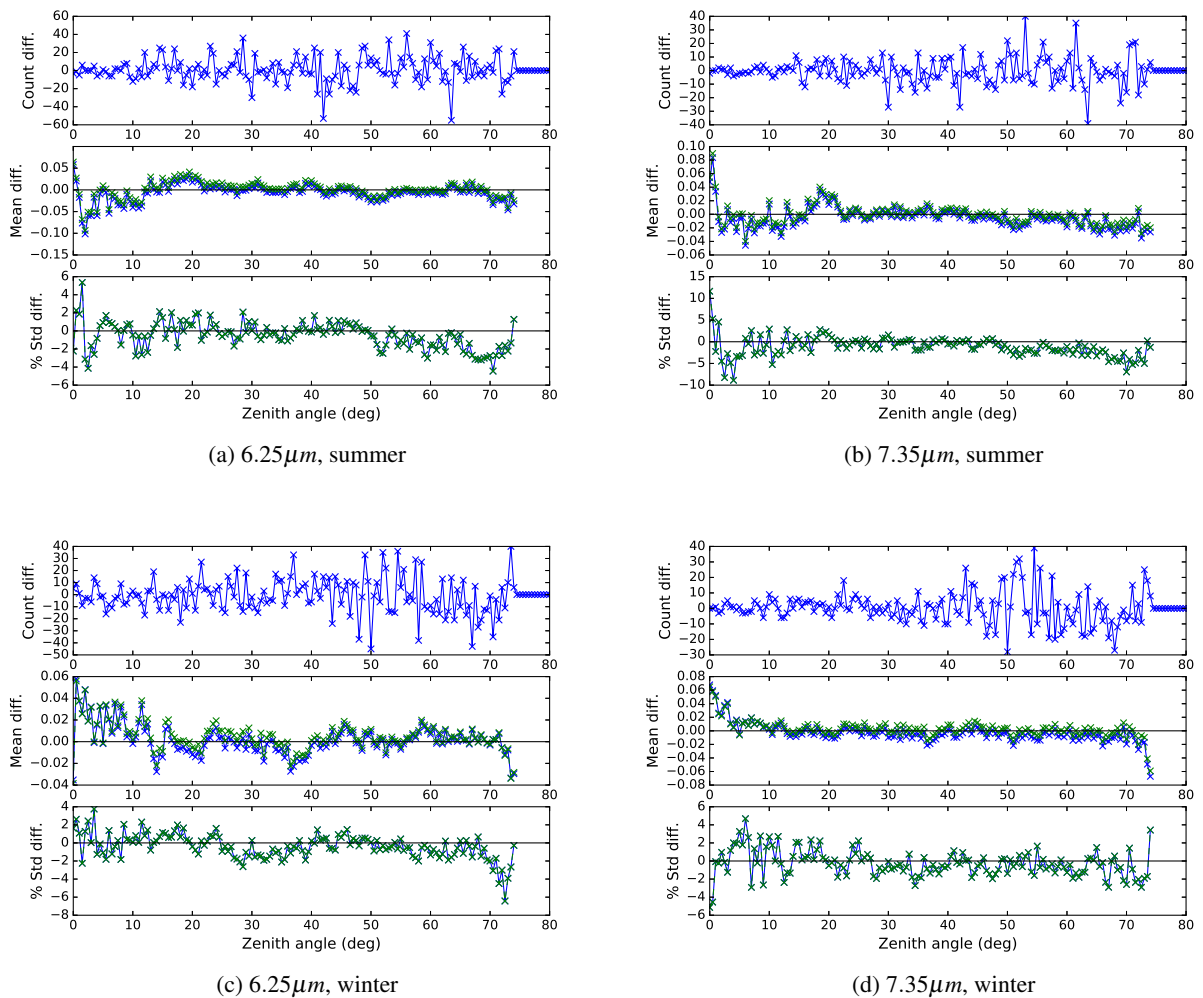


Figure 35: Differences in Meteosat-10 first guess departures when slant-path processing is applied in an the experiment (convention is experiment minus reference). The standard deviation differences are shown as percentages, i.e.  $100\% \times (\text{experiment} - \text{control}) / \text{control}$ . The channels and seasons are consistent with Figure 34.

From Figure 35 it can be seen that there are small changes to the number of observations that are used between the experiment and control, as a result of more or fewer observations exceeding quality control thresholds. There are also differences in the bias characteristics of the forward-modelled brightness temperatures, but the key difference is that for large zenith angles, i.e. larger than about  $65^\circ$ , there is,

in general, a reduction in the standard deviations of the first guess departures, as would be expected. However, as stated above, this reduction is due to a combination of improved forward-modelling as well as the indirect impact via the cycling nature of experiment.

## 2.3 Diagnosed inter-channel error correlations

### 2.3.1 Background

The current assimilation methodology for the geostationary radiances includes the prescription that the observation errors for the water vapour channels are 2K, and inter-channel error correlations do not exist. We know, however, that the vertical intervals of the atmosphere measured by adjacent water vapour channels overlap. Therefore, even if the measurement errors themselves are not correlated, the forward-modelling of these overlapping vertical bands will result in errors of representation that are likely to be correlated. A widely used method of obtaining an estimate of observation errors was proposed by Desroziers (Desroziers et al. [2005]), and this method has been widely used to diagnose inter-channel observation error covariances for both infrared and microwave passive radiances (Bormann and Bauer [2010], Bormann et al. [2011, 2015], Weston et al. [2014]). The notation used in the original paper is convenient; the difference between two vectors (where state-space quantities are mapped into observation space) is given by  $\mathbf{d}$  where the quantity denoted by the subscript is subtracted from the quantity denoted by the superscript. For example,  $\mathbf{d}_b^o = \mathbf{y} - H(\mathbf{x}_b)$ ,  $\mathbf{d}_a^o = \mathbf{y} - H(\mathbf{x}_a)$  and  $\mathbf{d}_b^a = H(\mathbf{x}_a) - H(\mathbf{x}_b)$ . Here,  $\mathbf{y}$  is the observation vector,  $\mathbf{x}_b$  is the background state vector,  $\mathbf{x}_a$  is the analysis state vector and  $H$  is the nonlinear observation operator. Given several assumptions, the diagnosed observation error covariance matrix is given by:

$$\mathbf{R}_{diag} = E \left[ \mathbf{d}_a^o (\mathbf{d}_b^o)^T \right]$$

where  $E[\cdot]$  is the expectation operator.

If the departure vectors are constructed to contain the brightness temperatures differences from each channel, then the resulting covariance matrix will have dimension  $m \times m$  where  $m$  is the number of channels. Here, we are interested solely in those channels which are currently being assimilated, i.e. the WV-sensitive channels.

### 2.3.2 Diagnosed R-matrices

Background and analysis departures were acquired for two periods; December 2016 and June 2017. The diagnosed covariance matrices (and corresponding correlation matrices) for the available instruments for these two periods are shown in Table 2 (along with a matrix for GOES-16 from a later period). These matrices have been rendered symmetric by calculating  $\mathbf{R}_{symm} = 0.5 \left( \mathbf{R}_{diag} + \mathbf{R}_{diag}^T \right)$ .

Satellite	Winter (cov)	Winter (corr)	Summer (cov)	Summer (corr)
GOES-13	0.73	N/A	0.74	N/A
GOES-15	0.70	N/A	0.70	N/A
Meteosat-7	0.59	N/A	N/A	N/A
Meteosat-8	N/A	N/A	$\begin{pmatrix} 0.55 & 0.22 \\ 0.22 & 0.44 \end{pmatrix}$	$\begin{pmatrix} 1 & 0.45 \\ 0.45 & 1 \end{pmatrix}$
Meteosat-10	$\begin{pmatrix} 0.46 & 0.20 \\ 0.20 & 0.30 \end{pmatrix}$	$\begin{pmatrix} 1 & 0.54 \\ 0.54 & 1 \end{pmatrix}$	$\begin{pmatrix} 0.43 & 0.18 \\ 0.18 & 0.29 \end{pmatrix}$	$\begin{pmatrix} 1 & 0.52 \\ 0.52 & 1 \end{pmatrix}$
Himawari-8	$\begin{pmatrix} 0.61 & 0.48 & 0.25 \\ 0.48 & 0.52 & 0.36 \\ 0.25 & 0.36 & 0.42 \end{pmatrix}$	$\begin{pmatrix} 1 & 0.85 & 0.50 \\ 0.85 & 1 & 0.78 \\ 0.50 & 0.78 & 1 \end{pmatrix}$	$\begin{pmatrix} 0.55 & 0.43 & 0.22 \\ 0.43 & 0.46 & 0.31 \\ 0.22 & 0.31 & 0.35 \end{pmatrix}$	$\begin{pmatrix} 1 & 0.86 & 0.51 \\ 0.86 & 1 & 0.78 \\ 0.51 & 0.78 & 1 \end{pmatrix}$

(a)

Satellite	Summer (cov)	Summer (corr)
GOES-16	$\begin{pmatrix} 0.39 & 0.33 & 0.18 \\ 0.33 & 0.35 & 0.25 \\ 0.18 & 0.25 & 0.28 \end{pmatrix}$	$\begin{pmatrix} 1 & 0.88 & 0.54 \\ 0.88 & 1 & 0.80 \\ 0.54 & 0.80 & 1 \end{pmatrix}$

(b)

Table 2: Desroziers-diagnosed observation error covariance (and corresponding correlation) matrices for (a) the water vapour channels of the geostationary radiances that were available for two seasons (December 2016 and June 2017) and for (b) the water vapour channels on GOES-16 from a month in 2018.

As a comparison, the current assumed covariance matrix has much larger diagonal values than any of the diagnosed matrices, i.e. for Himawari-8 we have:

$$\mathbf{R}_{\text{himawari}} = \begin{pmatrix} 4 & 0 & 0 \\ 0 & 4 & 0 \\ 0 & 0 & 4 \end{pmatrix}$$

There are some interesting similarities between these matrices. For example, the correlation values are fairly consistent for equivalent channel combinations of each of the instruments, though some of them are very large; up to 0.86. Also, for each instrument the covariance and correlation values are quite similar for the two seasons (though Himawari-8 shows the largest differences between the seasons). The values of the variances of similar channels are, however, quite different for the various satellites, with GOES-13 having the largest diagnosed error, and Meteosat-10 having the lowest. There are several possible reasons for these differences, but these will not be investigated further; we shall use the diagnosed covariances as a starting point for improving the assumed observation errors that are used in the 4D-Var assimilation.

### 2.3.3 Error scaling and impact

Experience from prior work in this area has shown that performing assimilation with the diagnosed observation error covariance matrices produced by this method results in degradations to forecast skill. In such cases, the error covariances need to be inflated, and then, improvements in impact may be attained (Bormann et al. [2015], Weston et al. [2014], Bormann et al. [2015], Weston et al. [2014]). This scaling can be achieved a number of ways, but the approach here is to apply scaling factors which preserve the inter-channel correlation structure. Inflating all the eigenvalues of the covariance matrix by the same scaling factor meets this requirement, and this is mathematically equivalent to scaling each element of

the original matrix by the same factor. The choice of scaling factor is not obvious. In fact, previous work (Bormann et al. [2015]) has determined the optimal scaling factor pragmatically by testing several factors and selecting the one which provides the largest improvement in some metric (or metrics) of forecast skill. We follow this approach here.

When the experiments were performed, the software to ingest inter-channel correlations was set up to work on a per-instrument basis. This is in the process of being extended to work on a per-satellite basis (Peter Weston, private communication), but here we use one matrix per instrument. Arbitrarily, the winter matrices were selected for testing, and the values from GOES-13 were used for all GOES-Imager instruments, and the values from Meteosat-10 were used for both SEVIRI instruments. Note that unlike the other instruments, for SEVIRI, observations of fully overcast scenes are also assimilated (i.e. the ASR product), and these overcast departures were included in the sample used to generate the diagnosed R-matrices. The experiments spanned the three-month period of 1/6/17 to 30/8/17 and the scaling factors considered were 1, 2, 4, 6 and 8 *in terms of variance* (1, 1.41, 2, 2.45 and 2.83 in terms of standard deviations). In the plots in this section, the variance scaling factors are quoted. Figure 36 shows the change in fits of first guesses and analyses to independent observations when the inter-channel error correlations are applied in active experiments with a range of scaling factors.

It can be seen that the fit to the first guesses of these observations is generally improved by the introduction of the correlated errors, but the ranking of the scaling factors is inconsistent in these plots, so it is not obvious from these which should be used. The change in vector wind forecasts for a range of lead times is shown in Figure 37, with verification having been performed against operational analyses.

For many of the subplots in Figure 37, the scaling factor of 6 shows the largest improvement, though these are generally not statistically significant improvements. Verification of other state variables show a very similar pattern. The scaling factor of 6 also shows the largest improvement in first guess fits to radiosonde temperatures in the southern hemisphere, so this is the factor that has been chosen for implementation. Furthermore, the change in RMS error of relative humidity, temperature and vector winds at 500hPa can be seen to improve significantly under the Himawari-8 disc for this scaling factor (results not shown). This is, perhaps, to be expected as neglecting error correlations for an instrument with three channels, with two of those correlated with a correlation coefficient of 0.86, is likely to be more suboptimal than, for example, neglecting correlations for SEVIRI which has smaller error correlations between the channels.

#### 2.3.4 Effect of scaling on increments

By introducing inter-channel observation error correlations, the question arises of whether the observations are being given more or less weight in the assimilation. This is a difficult question to answer for two reasons; firstly the structure of the covariance matrix is not straightforward to interpret in terms of its overall magnitude, and secondly that when the analysis step is performed, the magnitude of the analysis increments will also depend the forward model and the background error covariance, and their interactions are not immediately obvious.

By considering the linear analysis step, we can see the importance of correctly accounting for observation errors. The analysis increment is

$$\mathbf{x}_a - \mathbf{x}_b = \mathbf{B}\mathbf{H}^T (\mathbf{H}\mathbf{B}\mathbf{H}^T + \mathbf{R})^{-1} (\mathbf{y} - \mathbf{x}_b)$$

Transform this into observation space and apply the Desroziers notation

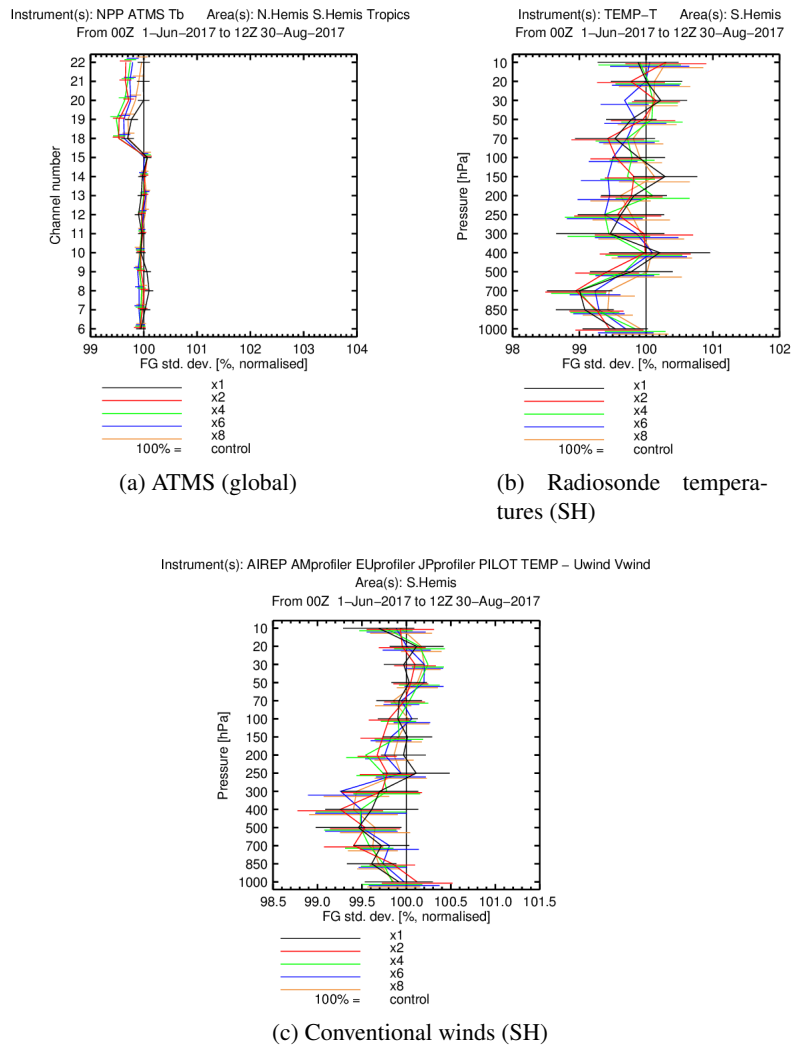


Figure 36: Changes in fit of first guesses to independent observations when the geostationary radiances are assimilated with correlated errors that have been scaled by various factors. The control uses 2K errors with no inter-channel error correlations.

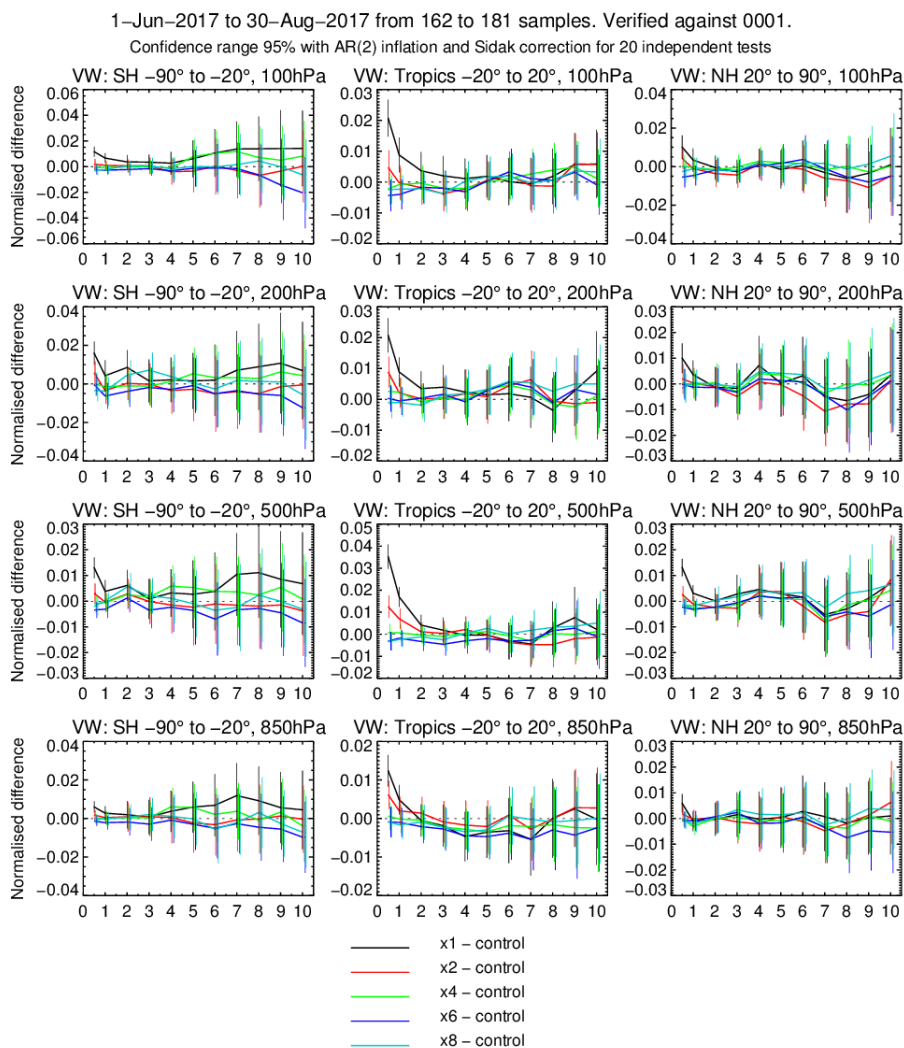


Figure 37: Change in vector wind RMS error verified against operational analyses for a range of lead times for the different scaling factors.

$$\mathbf{d}_b^a = \mathbf{HBH}^T (\mathbf{HBH}^T + \mathbf{R})^{-1} \mathbf{d}_b^o$$

Now take the covariance of this:

$$\overline{\mathbf{d}_b^a (\mathbf{d}_b^a)^T} = \mathbf{HBH}^T (\mathbf{HBH}^T + \mathbf{R})^{-1} \overline{\mathbf{d}_b^o (\mathbf{d}_b^o)^T} (\mathbf{HBH}^T (\mathbf{HBH}^T + \mathbf{R})^{-1})^T$$

This represents the expected size of the analysis increments (including correlations). Now, we are interested in assessing the magnitude of these increments for different values of  $\mathbf{R}$ . In order to ascertain the sensitivity of the increments to the choice of  $\mathbf{R}$  we will fix  $\mathbf{HBH}^T$  as that diagnosed by the Desroziers method. Table 3 shows the increment covariances for various choices of  $\mathbf{R}$  for the two SEVIRI WV channels, including 2K uncorrelated errors, the raw Desroziers-diagnosed matrix, and this matrix multiplied by several scaling factors. The determinant of each analysis increment covariance matrix is shown as this is indicative of the square root of the “volume” of constant probability density in which the increments lie (the determinant of a matrix is the product of its eigenvalues). The logarithm of this value (a form of the Shannon entropy Rodgers [2000]) is also shown.

$\mathbf{HBH}^T$	$\overline{\mathbf{d}_b^o (\mathbf{d}_b^o)^T}$	$\mathbf{R}$	$\overline{\mathbf{d}_b^a (\mathbf{d}_b^a)^T}$	$\det (\overline{\mathbf{d}_b^a (\mathbf{d}_b^a)^T})$	$\ln (\det (\overline{\mathbf{d}_b^a (\mathbf{d}_b^a)^T}))$
$\begin{bmatrix} 0.82 & 0.43 \\ 0.43 & 0.40 \end{bmatrix}$	$\begin{bmatrix} 1.28 & 0.63 \\ 0.63 & 0.70 \end{bmatrix}$	$\begin{bmatrix} 4 & 0 \\ 0 & 4 \end{bmatrix}$	$\begin{bmatrix} 0.06 & 0.03 \\ 0.03 & 0.02 \end{bmatrix}$	$2.31 \times 10^{-5}$	-10.68
$\begin{bmatrix} 0.82 & 0.43 \\ 0.43 & 0.40 \end{bmatrix}$	$\begin{bmatrix} 1.28 & 0.63 \\ 0.63 & 0.70 \end{bmatrix}$	$\begin{bmatrix} 0.55 & 0.22 \\ 0.22 & 0.44 \end{bmatrix}$	$\begin{bmatrix} 0.46 & 0.26 \\ 0.26 & 0.18 \end{bmatrix}$	$1.92 \times 10^{-2}$	-3.95
$\begin{bmatrix} 0.82 & 0.43 \\ 0.43 & 0.40 \end{bmatrix}$	$\begin{bmatrix} 1.28 & 0.63 \\ 0.63 & 0.70 \end{bmatrix}$	2 $\begin{bmatrix} 0.55 & 0.22 \\ 0.22 & 0.44 \end{bmatrix}$	$\begin{bmatrix} 0.24 & 0.13 \\ 0.13 & 0.09 \end{bmatrix}$	$3.53 \times 10^{-3}$	-5.65
$\begin{bmatrix} 0.82 & 0.43 \\ 0.43 & 0.40 \end{bmatrix}$	$\begin{bmatrix} 1.28 & 0.63 \\ 0.63 & 0.70 \end{bmatrix}$	4 $\begin{bmatrix} 0.55 & 0.22 \\ 0.22 & 0.44 \end{bmatrix}$	$\begin{bmatrix} 0.10 & 0.06 \\ 0.06 & 0.04 \end{bmatrix}$	$4.42 \times 10^{-4}$	-7.72
$\begin{bmatrix} 0.82 & 0.43 \\ 0.43 & 0.40 \end{bmatrix}$	$\begin{bmatrix} 1.28 & 0.63 \\ 0.63 & 0.70 \end{bmatrix}$	6 $\begin{bmatrix} 0.55 & 0.22 \\ 0.22 & 0.44 \end{bmatrix}$	$\begin{bmatrix} 0.05 & 0.03 \\ 0.03 & 0.02 \end{bmatrix}$	$1.14 \times 10^{-4}$	-9.08
$\begin{bmatrix} 0.82 & 0.43 \\ 0.43 & 0.40 \end{bmatrix}$	$\begin{bmatrix} 1.28 & 0.63 \\ 0.63 & 0.70 \end{bmatrix}$	8 $\begin{bmatrix} 0.55 & 0.22 \\ 0.22 & 0.44 \end{bmatrix}$	$\begin{bmatrix} 0.03 & 0.02 \\ 0.02 & 0.01 \end{bmatrix}$	$4.16 \times 10^{-5}$	-10.09
$\begin{bmatrix} 0.82 & 0.43 \\ 0.43 & 0.40 \end{bmatrix}$	$\begin{bmatrix} 1.28 & 0.63 \\ 0.63 & 0.70 \end{bmatrix}$	10 $\begin{bmatrix} 0.55 & 0.22 \\ 0.22 & 0.44 \end{bmatrix}$	$\begin{bmatrix} 0.02 & 0.01 \\ 0.01 & 0.01 \end{bmatrix}$	$1.86 \times 10^{-5}$	-10.89

Table 3: This table shows the covariance of analysis increments for assimilating SEVIRI WV channels using a range of R-matrices, including uncorrelated errors and Desroziers-derived errors with a range of scaling factors. The background error covariances are fixed, as derived from the Desroziers method. The determinant of the analysis increment covariance matrix and the Shannon entropy are shown as scalar diagnostics.

It can be seen that the magnitude of the determinant decreases as the scaling factor is increased, as we would expect. In fact, a scaling factor of approximately 10 (in units of variance) is required in order to reduce the average magnitude of the increments to that of the uncorrelated case. The scaling factor selected for implementation is 6, hence this results in the observations being given more weight than they were when the correlations were neglected. It is interesting to compare the analysis increment covariances for this case with the uncorrelated case. The increments using the correlated R-matrix have smaller diagonal elements and the inter-channel correlations are also reduced (i.e. even when  $\mathbf{R}$  is uncorrelated, correlations in  $\mathbf{B}$  dominate the correlations in the analysis increments).

Another interesting metric is the concept of the *effective number of independent observations*. If two observations have uncorrelated uncertainties, they will provide two pieces of information, but if the errors are 100% correlated with each other, only one piece of information will be provided, i.e. if one observation is known, the other is also known from the knowledge of their perfect correlation.

### 3 Future work

It is intended that GOES-16 CSR data will be assimilated operationally as soon as possible, assuming that forecast impact experiments show the improvements that would be expected. There are some potential plans for the GOES-16 CSR data to be based on a more sophisticated cloud mask (Andy Heidinger, private communication), so in this event, an investigation of these data would be necessary. Once an “official” cloud mask has been selected, it may be worthwhile to consider assessing the ASR product with a view to assimilating this instead. Looking further ahead, GOES-17 is due to replace GOES-15 as the GOES-WEST service, so these data will need to be assessed prior to being assimilated.

GOES-16 offers a unique possibility for future research, whereby it provides CSR data from the full disc every 15 minutes. Observational data with this degree of spatial coverage and temporal resolution offers a potentially new opportunity for 4D-Var data assimilation. It has already been shown that the impact on wind scores does not become saturated as the temporal frequency of observations is increased to hourly observations Peubey and McNally [2009], so this study can now be extended to observations which are valid every 15 minutes.

Another avenue of research to pursue involves prescribing observation errors that vary throughout the assimilation window (Tony McNally, private communication). The rationale for this is that the assumed R-matrix ought to capture errors in both the observations and in the forward modelling. In a 4D-Var system, the forward-modelling includes the integration of the forecast model, whose errors grow with time, as can be seen from the increase in first guess departure standard deviations throughout the assimilation window for the geostationary radiances. Accounting for model error in this sense Howes et al. [2017] is in some ways an alternative approach to the weak-constraint formulation. The inflation of observation errors throughout the assimilation window is technically straightforward, so this will be investigated, though temporal correlations in the errors will be neglected, at least initially.

The Chinese geostationary satellite FY-4A was launched in December 2016, and carries the hyperspectral infrared instrument GIIRS — the first of its kind in such an orbit. Obtaining and analysing data from this satellite is a priority. This is particularly important as the experience gained in implementing GIIRS will be valuable in preparing to assimilate data from the Infra Red Sounder (IRS) instrument on EUMETSAT’s Meteosat Third Generation (MTG) series of satellites.

## Acknowledgements

Many thanks to the following for their varied contributions and assistance: Tony McNally, Cristina Lupu, Pete Weston, Peter Lean, Niels Bormann, Julie Letertre-Danczac, Tim Hewison, Arthur de Smet, Tom King, Qiang Zhao, Yusuke Ioka, Sean Healy, Katie Lean, Crispian Batstone, Ruth Taylor, Fernando Prates, Ioannis Mallas, Gabor Radnoti and John Hodkinson.

## References

- N. Bormann. Slant path radiative transfer for the assimilation of sounder radiances. *ECMWF Technical Memorandum 782*, 2016.
- N. Bormann and P. Bauer. Estimates of spatial and interchannel observation-error characteristics for

- current sounder radiances for numerical weather prediction. I: Methods and application to ATOVS data. *Quarterly Journal of the Royal Meteorological Society*, 136(649):1036–1050, 2010.
- N. Bormann, S. B. Healy, and M. Hamrud. Assimilation of MIPAS limb radiances in the ECMWF system. II: Experiments with a 2-dimensional observation operator and comparison to retrieval assimilation. *Quarterly Journal of the Royal Meteorological Society*, 133(623):329–346, 2007.
- N. Bormann, A.J. Geer, and P. Bauer. Estimates of observation-error characteristics in clear and cloudy regions for microwave imager radiances from numerical weather prediction. *Quarterly Journal of the Royal Meteorological Society*, 137(661):2014–2023, 2011.
- N. Bormann, M. Bonavita, Dragani R., R. Eresmaa, M. Matricardi, and A. McNally. Enhancing the impact of IASI observations through an updated observation error covariance matrix. *ECMWF Technical Memorandum 756*, July 2015.
- G. Desroziers, L. Berre, B. Chapnik, and P. Poli. Diagnosis of observation, background and analysis-error statistics in observation space. *Quarterly Journal of the Royal Meteorological Society*, 131(613):3385–3396, 2005.
- EUMETSAT. MSG Meteorological Products Extraction Facility Algorithm Specification Document. *EUMETSAT EUM/MSG/SPE/022 v7b*, 2015.
- EUMETSAT. MSG Level 1.5 Image Data Format Description. *EUMETSAT EUM/MSG/ICD/105 v8*, 2017.
- K. E. Howes, A. M. Fowler, and A. S. Lawless. Accounting for model error in strong-constraint 4D-Var data assimilation. *Quarterly Journal of the Royal Meteorological Society*, 143(704):1227–1240, 2017.
- C Köpken, J-N. Thépaut, and G Kelly. Assimilation of Geostationary WV Radiances from GOES and Meteosat at ECMWF. *EUMETSAT/ECMWF Fellowship Programme Research Report No. 14*, 2003.
- J. Letertre-Danczak. Monitoring and operational assimilation of Himawari-9 clear-sky geostationary radiances. *ECMWF Research Department Memorandum RD16-029*, 2016a.
- J. Letertre-Danczak. An evaluation of radiance data from Meteosat-11. *ECMWF Research Department Memorandum RD16-052*, 2016b.
- C. Lupu and A.P. McNally. Assimilation of cloud-affected radiances from Meteosat-9 at ECMWF. *EUMETSAT/ECMWF Fellowship Programme Research Report No. 25*, 2012.
- R. Munro, C. Köpken, G. Kelly, J-N. Thépaut, and R. Saunders. Assimilation of Meteosat radiance data within the 4D-Var system at ECMWF: Data quality monitoring, bias correction and single-cycle experiments. *Quarterly Journal of the Royal Meteorological Society*, 130(601):2293–2313, 2004.
- C. Peubey and A.P. McNally. Characterization of the impact of geostationary clear-sky radiances on wind analyses in a 4D-Var context. *Quarterly Journal of the Royal Meteorological Society*, 135:1863–1876, 10 2009.
- C.D. Rodgers. *Inverse Methods for Atmospheric Sounding*. World Scientific, 2000.
- P. P. Weston, W. Bell, and J. R. Eyre. Accounting for correlated error in the assimilation of high-resolution sounder data. *Quarterly Journal of the Royal Meteorological Society*, 140(685):2420–2429, 2014.